Gap properties of helical edge states in two-dimensional topological insulators with time-dependent magnetic impurities

by Simon Wozny

LUND
UNIVERSITY

Department of Physics
Solid State Physics

Thesis for the degree of Master of Science
HT19 and VT20

Thesis supervisors:
Martin Leijnse (Lund University)
Sigurður I. Erlingsson (Reykjavik University)

Examiner:
Claudio Verdozzi (Lund University)

June 15, 2020

Abstract

The quantum mechanical equivalent of the classical Hall effect can lead to interesting results in solid state physics. A similar effect, that has received attention in recent years, occurs when large spin-orbit coupling is present in a material, the so-called quantum-spin Hall effect. In two-dimensional materials it leads to so-called helical edge states that exhibit counter-propagating electron states located at the edge with spin-momentum locking protected by time-reversal symmetry. That means, different spin species travel in different directions along the edge and cannot be scattered into each other unless time-reversal is broken by a magnetic contribution. Two-dimensional materials hosting these quantum spin Hall states are commonly called two-dimensional topological insulators.

In this thesis we investigate the electronic structure of the edge states in the presence of magnetic impurities with rotating magnetic moments. Since they break time reversal symmetry, the impurities lead to backscattering and the density of states can be altered drastically in their presence. To calculate the time-averaged density of states, a Floquet-like approach is applied to the single-particle Green's function of the 2×2 effective edge Hamiltonian of the Bernevig-Hughes-Zhang model with impurities. The rotation of the impurities in the x-z-plane leads to the density of states transitioning between a gapped and an ungapped state, which in turn leads to drastically different shapes of the density of states depending on the driving frequency.

A numerical model is derived and criteria for choosing reasonable numerical cut-offs are given. The resulting density of states looks different for different driving frequencies. Slow driving, compared to a time scale defined by the magnetic impurity strength, leads to a density of states comparable to the average over static impurities for different impurity orientations. Fast driving effectively does not alter the low energy density of states, leaving it constant around the center, with distinct resonances at energies related to the driving frequency. Driving with frequencies around the time scale defined by the impurities leads to different results, exhibiting additional resonances, broadened due to the impurity nature of the system.

Contents

Acknowledgments

There is a good number of people involved, in one way or another, in making this thesis project a very enjoyable time. Firstly, a big thank you to my supervisors Martin and Siggi. Thank you Martin, for taking me in with the project, introducing me to the group and always giving me the possibility to participate. I always felt really welcome in the group! Of course, this whole project would not have been possible without Siggi. Thank you for supporting me since my first bachelor thesis and introducing me to the whole topic in the first place.

I would also like to thank the rest of the group for making me feel welcome, always keeping an open door and never making me feel like "just another thesis student".

There are always more people to thank than there is time for. I want to thank everyone from the degree student office, for always being up for a chat, a coffee break or helping with whatever small things came up. A final thank you goes everyone else that supported me during the thesis project, be it with moral support, proofreading, virtual coffee breaks or whatever else made life better.

Publication of the results

Following this thesis project, the aim is to write a manuscript for the purpose of publishing it in a scientific journal. The results of the thesis will be the foundation upon which the publication will be based.

Abbreviations

2D two-dimensional

3D three-dimensional

BHZ Bernevig-Hughes-Zhang

QH Quantum Hall

QSH quantum-spin-Hall

TI topological insulator

TRS time-reversal symmetry

1 Introduction

One of the largest fields of physics is condensed matter physics. It generally deals with the physics of matter made up of a big number of constituents. Relatively recently the field of topology, topological states and topological phase transitions has arisen as an area of interest within condensed matter physics. In this introduction we will give a short overview of the effects and developments within this area of condensed matter physics that are relevant for this thesis.

1.1 The quantum Hall effect and Topology

The quantum mechanical equivalent of the classical Hall effect that leads to a quantized conductance was predicted in 1975 [1] and measurements in two-dimensional (2D) electron systems were undertaken in 1978 [2]. The classical Hall effect can be seen in a conducting plate with a current in one direction and a magnetic field perpendicular to the plate. This leads to the so-called Hall voltage, which can be understood classically by considering the Lorentz force acting on the moving charge carriers. It is perpendicular to the direction of movement of the carriers and thus leads to a potential difference across the plate, the Hall voltage. In strong magnetic fields the electrons are forced onto circular orbits and a quantum mechanical treatment leads to quantized orbits with discrete energies, the so-called Landau levels. This leads to the so-called chiral edge states [3], that can be understood in a semi classical picture. On the edges of the plate the charge carriers can not complete the orbit and are reflected back into the plate, where they again follow the circular orbit and "bounce" along the edge in these so-called skipping orbits [4]. This is visualized in Fig. 1.1. Transport in Quantum Hall (QH) systems takes place via the chiral edge channels, which do not take into account the spin of the carriers. Because of the discrete Landau levels the conductance is quantized. In 1980 the exact quantization of the Hall conductance was measured [5] and the QH effect thereby confirmed. Due to the required presence of a magnetic field for the QH effect, time-reversal symmetry (TRS) is explicitly broken in these systems.

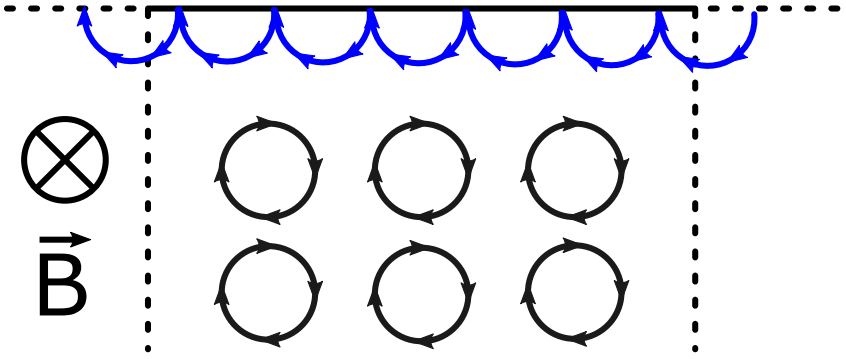

FIG. 1.1: Edge channels in QH system due to circular orbits "bouncing" along the edge.

Another property of the chiral edge states is that they appear within the bulk gap in the spectrum of the system that is opened by the external magnetic field. The band structure also provides an entry point to the notion of topology within solid state physics. In mathematics one of the most commonly employed examples of topology is the equivalence of a coffee mug and a donut. These two objects can be classified by the number of holes in their 2D surface, and can be transformed into each other smoothly. Similarly, the gaps

in the spectrum can be classified by whether they can be transformed into each other by a smooth deformation of the bands or not [6]. This concept holds the key to classifying the states responsible for the quantized Hall conductance mentioned earlier. In the classical notion the order parameters defined by spontaneous symmetry breaking assume a non-zero expectation value in an ordered phase. The transition of this order parameter from zero to a finite value defines a phase transition of matter. Matter in a QH state could not be classified according to the classically known order parameters [5], meaning there was no known order parameter that changed when transitioning from a non-QH to a QH state. Instead the notion topological invariants had to be introduced to distinguish these states and the edge states can only exist in a certain class of topologically distinct gaps.

1.2 Topological insulators

In so called quantum-spin-Hall (QSH) systems there are two counter-propagating edge states. In a picture similar to the semi-classical one for QH systems the circular orbits are caused by spin-orbit coupling in the material and thus the two spin species travel in different directions on the circular orbits. Consequently, on the edges two spin polarized channels propagating in opposite directions are formed. Such states are called helical edge states [6]. Figure 1.2 schematically shows these states on the edge of a 2D host material. A difference to the QH effect is the opposite direction of propagation of the two spin channels (red/blue) indicated by the black arrows.

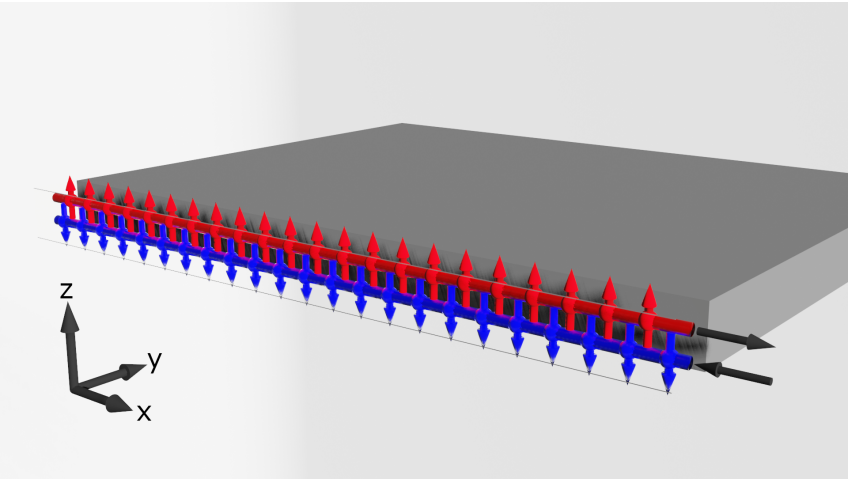

FIG. 1.2: Edge channels carrying different spin species (red/blue) on the edge of a 2D material.

The QSH effect, in contrast to the QH effect, conserves TRS due to the channels having opposite propagation direction. It is caused by spin-orbit coupling and thus can be realized without an external magnetic field, but requires materials with big spin-orbit coupling. It was proposed in 2006 [7] and first measured in 2007 [8] in HgTe/(Hg,Cd)Te quantum wells. Essentially the 2D host material consists of two CdTe layers with a HgTe layer in between, leading to a inversion of valence and conduction band in the HgTe layer at a critical thickness. This means that e.g. bands belonging to a certain symmetry classes now act as valence band, while in bulk they would lay energetically higher and act as conduction band. Consequently, the conduction and valence band can belong to different symmetry classes, depending on the quantum well geometry [6]. These types of 2D materials, naturally hosting the QSH states, are called 2D topological

insulators (TIs). The edge channels can be described by the one-dimensional (1D) massless Dirac equation [6, 9], which again highlights the counter-propagating nature of the edge channels visualized in Fig. 1.2. Following the predictions, various measurements on 2D TI HgTe systems, e.g. resistance measurements [10, 11] and current imaging [12], have been undertaken and the predicted properties have been confirmed [13]. Following the HgTe related discoveries InAs/GaSb/AlSb Type-II semi-conductor quantum wells were also predicted to host QSH states in 2008 [14]. Subsequently, in these systems resistance measurements [15–17] and edge current imaging experiments [18] were performed. The 2D TI model can also be generalized to three-dimensional (3D) materials that host surface states, for example in BiSb alloys [6, 19, 20]. Furthermore, efforts are made to demonstrate a quantum mechanical analogue to the anomalous Hall effect, the quantum-anomalous Hall effect, in 3D and 2D systems [21–24]. The anomalous Hall effect is similar to the Hall effect but is not caused by an external magnetic field, but by a magnetization of the material. The quantum-anomalous Hall effect again is the quantum mechanical version with quantized electron orbits caused by the magnetization [25, 26].

TIs in general promise a great range of applications in various areas. First of all, dissipationless transport via the edge channels opens up possibilities in low-power information processing and spintronics [13], for example the behavior of field-effect transistors made from 3D TIs have been studied recently [27]. Aside from that, by coupling superconductors to TIs, systems that should support Majorana bound states can be achieved and applications for topological quantum computing are proposed [6, 28]. Majorana bound states are quasi-particles, associated with super-conductivity, that are their own anti-particle and follow non-abelian exchange statistics. In addition to the electronic properties, TIs also show interesting optical properties , like non–isotropic and ultrahigh refractive indices that can find application in optoelectronic and optical devices [29]. TI based materials have also been used to realize nanometric holograms , projections of images that appear when a carefully designed nano structure is illuminated by a laser and viewed from a certain angle. These promise advances for example in data storage devices [30].

1.3 Impurities, scattering and opening of bandgaps in TIs

Another aspect in TI systems are the effects of impurities on the QH and QSH states. While in reality it is very hard to produce completely clean systems and foreign atoms in the crystal lattice act as impurities, often these foreign atoms are even desired and purposefully introduced into the system. This is called doping and is usually done to alter the electronic properties of the system. In this project we will concern ourselves with these doping impurities. However, sometimes also local perturbations, for example by an extremely focused laser, can be viewed as single impurities [31]. Since the TI edge states are protected by TRS, potential disorder does not lead to a gap in the density of states. Magnetic contributions break TRS and can lead to a gap, depending on their orientation. For doping impurities it is possible to dope certain TI materials during the growth with Mn atoms that can be magnetically aligned in the process [32]. For this kind of magnetically aligned, static impurities there have been theoretical studies on 3D [33] as well as on 2D TI systems [34]. Magnetic impurities explicitly break TRS and in both cases magnetically aligned impurities lead to a gap in the density of states, similar to the gap formed by an external magnetic field. Furthermore, in both the mentioned studies the gap has been shown to close for rising electric potential of the impurities. There are

other gap opening mechanisms, for example current induced gaps in 3D TIs [35] or finite size effects in 2D strips [36] which will not be considered here.

This project focuses on randomly placed, dynamic, aligned magnetic impurities. More specifically, we consider impurities located on the edge channels of 2D TIs, harmonically rotating in the x-z-plane. The aim is to investigate the time-averaged density of states in this system. Figure 1.3 schematically shows this set-up with the edge channels (red/blue) and the impurities (yellow) placed on them, rotating in the x-z-plane (indicated by the black arrows). This rotation of the impurities could for example be experimentally realized by ferromagnetic resonance. Similar to nuclear magnetic resonance, ferromagnetic resonance describes the precession of the magnetization of a material induced via an external field. Ferromagnetic resonance has been used to probe Mn doped semiconductors [37]. Another way to induce rotating magnetization is free precession of Mn, but the precession is rather quickly damped [38]. The magnetization is given by the impurities and thus the precession of it indicates a rotation of the impurities magnetic momenta , which we assume to be in phase.

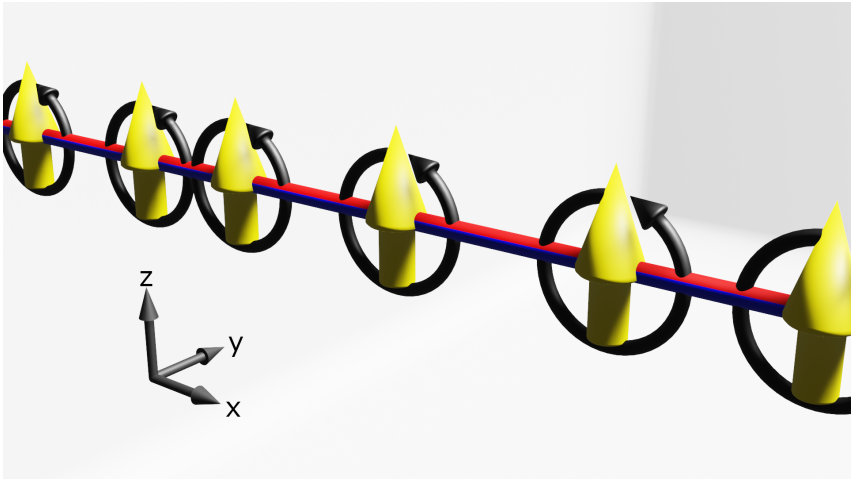

FIG. 1.3: Randomly placed, aligned rotating magnetic impurities (yellow) on the 1D Edge channels (red/blue).

The choice of the plane of rotation in our system is not arbitrary. A magnetization in the direction of the spin-polarization of the edge states will not open a gap in the edge channel density of states whereas a magnetization perpendicular to the polarization will open a gap. The rotation between these two orientations should thus lead to the density of states transitioning between an ungapped and a gapped state. This will significantly alter the time-averaged density of states. The framework to find the density of states will be Green's function theory [39, 40] and the time dependence will be treated employing methods related to Floquet theory [41–48]. Note here, that we are working with intrinsic TIs and are not looking at so called Floquet-TIs [49] which are materials externally driven into a topological phase. Green's functions and Floquet theory will be introduced in section 2, along with other theoretical tools. In section 3 a very general matrix equation to find the Green's function for a driven system will be derived, before discussing the application to the 2D TI system in section 4 along with numerical considerations. The results and discussion can be found in section 5, before we give a brief summary and an outlook in section 6. The numerical code and various detailed calculations and additional plots can be found in the appendices after the references.

2 Theoretical methods and model

In this section we will introduce the most important concepts used to perform analytical and numerical calculations on 2D TI systems. First, we will introduce some general basics of Green's function theory, the main tool used to deduce the density of states. Then we will give an introduction to the Floquet formalism, followed by a closer look at the Hamiltonian of 2D TIs, namely the BHZ model, and an application of Green's function theory to it.

2.1 Green's function

One of the most popular equations in quantum physics is the time-dependent Schrödinger equation

$$(H - \mathrm{i}\hbar\partial_t)\psi(t) = 0. \tag{2.1}$$

It describes the time-evolution of a wave-function $\psi(t)$ in a system defined by the Hamiltonian H. Regardless whether the Hamiltonian is a differential operator, the time derivative makes the Schrödinger equation a differential equation. In order to solve this class of problems, a rich mathematical toolkit has been developed. A popular tool in this kit are the single-particle Green's functions of the many-body system. Here we will give a short introduction to the most relevant aspects following Refs. [39, 40]. The particularly relevant retarded Green's function is defined as

$$g^R(\vec{r}, \sigma, t; \vec{r}', \sigma', t') = -\mathrm{i}\theta(t - t') \left\langle \{\Psi_\sigma(\vec{r}, t), \Psi^\dagger_{\sigma'}(\vec{r}', t')\} \right\rangle \tag{2.2}$$

in it's general form for Fermions. Here $\Psi^\dagger_\sigma(\vec{r}, t)$ and $\Psi_\sigma(\vec{r}, t)$ are quantum field creation and annihilation operators at position $\vec{r}$ and time t with spin σ in second quantization and $\{\cdot, \cdot\}$ denotes the anti-commutator. In the non-interacting case this is equivalent to defining it as a solution of the so-called equation of motion,

$$[i\hbar\partial_t - H(\vec{r})]\, g(\vec{r}, t; \vec{r}', t') = \delta(t - t')\delta(\vec{r} - \vec{r}'), \tag{2.3}$$

where the spin indices σ, σ' lead to a matrix structure of the Green's function. The solution corresponding to the retarded Green's function can be written as

$$g^R(\vec{r}, t; \vec{r}', t') = -\mathrm{i}\theta(t - t') \left\langle \vec{r} \right| e^{-\mathrm{i}H(t-t')} \left| \vec{r}' \right\rangle . \tag{2.4}$$

This form highlights the similarity of the two formulations. It also explains the name *retarded* Green's function when looking at how it describes the time-propagation of a known wave function ψ at time t' via the integral equation

$$\psi(\vec{r}, t) = \int \mathrm{d}\vec{r}'\, g^R(\vec{r}, t; \vec{r}', t')\psi(\vec{r}', t'). \tag{2.5}$$

The time evolution via the retarded Green's function depends on the wave function at an earlier time t'. This is also the origin of the name propagator, often used for the retarded Green's function. Furthermore, this shows that the retarded Green's function is of interest for physicists since it contains all the information about the time-evolution and dynamics of a physical system. Physically Eq. (2.5) describes, what happens to a state or particle inserted into an empty many-body system at time t'. It is the so-called *single particle Green's function of the many body system.*

Mathematically speaking, the Green's function is a fundamental solution to the Schrödinger equation and as such we can often employ mathematical tools to find it. One of the most important approaches is the Fourier transformation to other coordinate systems, e.g. from the real-space to the momentum domain or the time to the energy-domain, since they convert derivatives to multiplications and Dirac-δ-functions to simple unit elements. These transformations sometimes allow to find Green's functions and will often be used in the following chapters. The main difficulty lies in the transformation back to the original coordinates and will typically involve residue calculus.

2.2 Spectral function and density of states

From the retarded Green's function in energy-momentum domain we can define the so-called spectral function as

$$A(k, E) = -2\mathrm{Im}\,\mathrm{Tr}\, g^R(k, E). \tag{2.6}$$

The trace describes the sum over all spin states, since for spinfull particles the Green's function will generally be a matrix. The spectral function describes the distribution of available states in the momentum domain at energy E and is similar to the band structure of a system. For example, for free electrons the spectral function will be $2\pi\delta(E - \mathcal{E}(k))$ where $\mathcal{E}(k)$ is the dispersion relation. Interactions, either between particles or in the system, e.g. scattering, will lead to a broadening of the δ-functions [39]. Nevertheless, the spectral function is an appropriate tool to visualize the spectral distribution of single electron states in heatmap-like plots, sometimes referred to as the low energy band structure [33].

This spectral distribution directly leads to the density of states, that can be seen as the number of available states in an energy interval. Thus, summing up all states at a given energy E and performing the continuous limit leads to the density of states

$$\mathcal{D}(E) = -2\sum_k \mathrm{Im}\,\mathrm{Tr}\, g^R(k, E) \to -\frac{1}{\pi}\int \mathrm{d}k\,\mathrm{Tr}\, g^R(k, E). \tag{2.7}$$

If the Green's function is found, for example, in real space as $g^R(x, x', E)$, instead of momentum space it simply reads

$$\mathcal{D}(E) = -\frac{1}{\pi}\mathrm{Im}\,\mathrm{Tr}\, g^R(x, x, E). \tag{2.8}$$

In this thesis we will be working with the single particle Green's function, which means that when referring to the density of states in the rest of this thesis we mean the density of *single-electron states*.

The spectral function and the density of states are important physical properties, since they can be experimentally accessed. For example tunnel spectroscopy can be used to measure the density of states [39] and recently angle-resolved photoemission spectroscopy in current carrying devices in non-equilibrium states has been used to measure the spectral function [50].

2.3 Floquet theory

The Green's function approach from section 2.1 also holds for an arbitrary time-dependent Hamiltonian, but in practice it is usually very difficult to find the Green's function. A

useful method, developed to understand time-periodic systems, is Floquet theory. Here we will briefly introduce this well known approach, following the descriptions for example in Refs. [41, 45, 47]. Compared to perturbation theory approaches it respects the periodicity of the driving and thus avoids so-called secular terms. Secular terms are linear or non-periodic in time and therefore do not respect the periodicity given by the driving. They typically appear in time-dependent perturbation theory [41].

Floquet theory gives a framework for solving the time-dependent Schrödinger equation for systems described by a time-periodic Hamiltonian $H(t+T) = H(t)$, suppressing all other coordinates, if not explicitly needed. This periodic time-dependence will in our case be given by the impurity potential, but in general there is no requirement for the periodicity to be contained in a potential. It can also be an intrinsic property of the Hamiltonian.

The dynamics of the system are then described by the time-dependent Schrödinger equation

$$(H(t) - \mathrm{i}\hbar\partial_t)\psi(t) = 0. \tag{2.9}$$

To solve this we can invoke the so-called Floquet theorem, that gives the existence of solutions of the form

$$\psi_\alpha(t) = \exp\left(-\mathrm{i}\frac{\epsilon_\alpha}{\hbar}t\right)\Phi_\alpha(t). \tag{2.10}$$

These are called Floquet-state solutions and consist of the quasi-energy exponential $\exp(-\mathrm{i}^{\epsilon_\alpha}/_{\hbar}t)$ and the time-periodic Floquet modes $\Phi_\alpha(t) = \Phi_\alpha(t+T)$. In a sense, the Floquet theorem is analogous to the Bloch theorem for periodic solids, but the periodicity lies in the time-coordinate instead of the spacial coordinate. Hence, in analogy to the quasi-momenta in the Bloch theorem, the ϵ_α are called the quasi-energies. The quasi-energies are unique up to multiples of the driving $\hbar\Omega = \hbar^{2\pi}/_T$ and we can, again similar to the Bloch theorem, define a Brillouin zone containing the unique eigenvalues like $-^{\hbar\Omega}/_2 \leq \epsilon_\alpha < {}^{\hbar\Omega}/_2$. The periodicity condition for the quasi-energies becomes clear, when we define the hermitian operator

$$\mathcal{H}(t) = H(t) - \mathrm{i}\hbar\partial_t, \tag{2.11}$$

giving the eigenvalue problem

$$\mathcal{H}(t)\Phi_\alpha(t) = \epsilon_\alpha\Phi_\alpha(t), \tag{2.12}$$

that is also called the Floquet equation. With $n \in \mathbb{Z}$ we see that $\Phi_{\alpha'} = \Phi_\alpha \exp(\mathrm{i}n\Omega t) = \Phi_{\alpha,n}$ solves Eq. (2.12) with a quasi-energy $\epsilon_{\alpha'} = \epsilon_\alpha + n\hbar\Omega$. Furthermore, these two solutions result in the same Floquet-state solution (2.10) and thus we can write a periodicity condition for the quasi-energies

$$\epsilon_{\alpha,n} = \epsilon_\alpha + n\hbar\Omega. \tag{2.13}$$

To solve the eigenvalue problem, it is useful to define a composite Hilbert space $\mathcal{R}\otimes\mathcal{T}$, composed of the space $\mathcal{R}$, spanned by the eigenfunctions of the time-independent part of the Hamiltonian $H(t) = H_0 + H_1(t)$ and the T-periodic functions $\mathcal{T}$. We can define the composite scalar product for functions $f, g \in \mathcal{R}\otimes\mathcal{T}$ as

$$\langle\langle f|g\rangle\rangle = \frac{1}{T}\int_0^T \mathrm{d}t \int \mathrm{d}q\, f^*(q,t)g(q,t). \tag{2.14}$$

If H_0 has a complete, orthonormal set of eigenfunctions ϕ_n, the Floquet modes can be decomposed in terms of these and as eigenvectors of $\mathcal{H}(t)$ they fulfill the orthonormality condition

$$\langle\langle \Phi_{\alpha,n} | \Phi_{\beta,m} \rangle\rangle = \delta_{\alpha,\beta}\delta_{m,n}. \tag{2.15}$$

Furthermore, they form a complete set in the composite space

$$\sum_{\alpha}\sum_{n} = \Phi^*_{\alpha,n}(q,t)\Phi_{\alpha,n}(q',t') = \delta(q-q')\delta(t-t'). \tag{2.16}$$

Solving the eigenvalue problem in the composite Hilbert space allows us to construct the Floquet-state solutions from the Floquet modes $|\Phi_\alpha(t)\rangle$ written in the space $\mathcal{R}$. These, in turn, give us the time evolution of any initial state as

$$|\psi(t)\rangle = \sum_{\alpha} c_\alpha \exp(-i\varepsilon_\alpha t/\hbar)\,|\Phi_\alpha(t)\rangle\,, \tag{2.17}$$

where $c_\alpha = \langle\Phi_\alpha(0)|\psi(0)\rangle$ for an initial state $|\psi(0)\rangle$ [41].

It is also possible to find the time-averaged Green's function from this approach either via a spectral representation of the propagator (see for example page 239 in Ref.[41]) or a matrix continued fraction approach on the Floquet Hamiltonian [44]. In the following paragraph the calculations to find the Floquet Hamiltonian in the composite space are performed for an exemplary two-level-system that we will later use in a similar form.

2.3.1 Two-level system

For a simple two-level system with harmonic perturbations a very general Hamiltonian reads

$$H(t) = H_0\sigma_z + \sum_{i=x,y,z} H_i\sigma_i \sin(\Omega t + \phi_i) \tag{2.18}$$

and can for example describe a spin-1/2-particle in a harmonically time-dependent magnetic field. It is also similar to the effective edge Hamiltonian of the BHZ model in momentum space for a fixed momentum and with a harmonic perturbation by a magnetic field. The Floquet theorem provides that solutions to the time-dependent Schrödinger equation are composed of time-periodic Floquet modes with the same period as the perturbation. That means we can Fourier-decompose the Floquet modes like

$$|\Phi_\alpha(t)\rangle = \sum_{n=-\infty}^{\infty} |c^n_\alpha\rangle \exp(\mathrm{i}n\Omega t), \tag{2.19}$$

where Ω is the driving frequency. We can now decompose the $|c^n_\alpha\rangle$ in terms of the complete set $|+\rangle\,, |-\rangle$ of eigenvectors of $H_0\sigma_z$ according to

$$|\Phi_\alpha(t)\rangle = \sum_{k=+,-}\sum_{n=-\infty}^{\infty} c^n_{\alpha,k}\,|k\rangle \exp(\mathrm{i}n\Omega t), \tag{2.20}$$

and inserting this into the Floquet-equation results in

$$\sum_{k=+,-}\sum_{n=-\infty}^{\infty}\left(H(t) - \mathrm{i}\hbar\frac{\partial}{\partial t}\right) c^n_{\alpha,k}\,|k\rangle \exp(\mathrm{i}n\Omega t) = \sum_{k=+,-}\sum_{n=-\infty}^{\infty} \varepsilon_\alpha c^n_{\alpha,k}\,|k\rangle \exp(\mathrm{i}n\Omega t). \tag{2.21}$$

Multiplying by $\langle k|\exp(-\mathrm{i}m\Omega t)$ and integrating over one driving period gives the matrix equation

$$\sum_{n=-\infty}^{\infty}\sum_{k=+,-}\langle\langle j,m|\,H(t)-\mathrm{i}\hbar\frac{\partial}{\partial t}\,|k,n\rangle\rangle\,c^n_{\alpha,k}=\varepsilon_\alpha c^m_{\alpha,j}, \tag{2.22}$$

where we introduced the notation $\langle k|\exp(-\mathrm{i}m\Omega t)=\langle k,m|$ and the composite space scalar product, denoted by $\langle\langle\ldots|\ldots|\ldots\rangle\rangle$ has been used. This is the eigenvalue problem we have to solve to find the quasi-energies. Defining

$$H^{m-n}=\frac{1}{T}\int_0^T \mathrm{d}t H(t)\exp(-\mathrm{i}(m-n)\Omega t), \tag{2.23}$$

we can calculate the matrix

$$\langle\langle j,m|\,H(t)-\mathrm{i}\hbar\frac{\partial}{\partial t}\,|k,n\rangle\rangle=\langle j|\,H^{m-n}\,|k\rangle+n\hbar\Omega\delta_{n,m}\delta_{j,k} \tag{2.24}$$

and use a eigenvalue/eigenfunction routine to find the quasi-energies. In the two-dimensional basis $|+\rangle,|-\rangle$ we can perform the integral to find H^{m-n}

$$\begin{aligned}
\langle j|\,H^{m-n}\,|k\rangle&=\frac{1}{T}\int_0^T \mathrm{d}t H(t)\exp(-\mathrm{i}(m-n)\Omega t)\\
&=\frac{1}{T}\int_0^T \mathrm{d}t\left(H_0\sigma_z\exp(-\mathrm{i}(m-n)\Omega t)\right.\\
&\quad\left.+\sum_{i=x,y,z}H_i\sigma_i\sin(\Omega t+\phi_i)\exp(-\mathrm{i}(m-n)\Omega t)\right)\\
&=H_0\sigma_z\underbrace{\frac{1}{T}\int_0^T \mathrm{d}t\exp(-\mathrm{i}(m-n)\Omega t)}_{=\delta_{n,m}}\\
&\quad+\sum_{i=x,y,z}H_i\sigma_i\frac{1}{T}\int_0^T \mathrm{d}t\underbrace{\sin(\Omega t+\phi_i)}_{=\frac{\exp(i(\Omega t+\phi_i))-\exp(\Omega t+\phi_i)}{2\mathrm{i}}}\exp(-\mathrm{i}(m-n)\Omega t)\\
&=H_0\sigma_z\delta_{m,n}-\frac{\mathrm{i}}{2}\sum_{i=x,y,z}H_i\sigma_i(\exp(\mathrm{i}\phi_i)\delta_{m,n+1}-\exp(-\mathrm{i}\phi_i)\delta_{m,n-1}).
\end{aligned} \tag{2.25}$$

This then leads to a matrix representation of the Floquet-Hamiltonian

$$\left(\begin{array}{c|c|c|c|c}
\ddots & \ddots & & & \\ \hline
\ddots & H_0\sigma_z-\hbar\Omega\sigma_0 & -\frac{\mathrm{i}}{2}\sum_i H_i\sigma_i\exp(\mathrm{i}\phi_i) & & \\ \hline
 & \frac{\mathrm{i}}{2}\sum_i H_i\sigma_i\exp(-\mathrm{i}\phi_i) & H_0\sigma_z & -\frac{\mathrm{i}}{2}\sum_i H_i\sigma_i\exp(\mathrm{i}\phi_i) & \\ \hline
 & & \frac{\mathrm{i}}{2}\sum_i H_i\sigma_i\exp(-\mathrm{i}\phi_i) & H_0\sigma_z+\hbar\Omega\sigma_0 & \ddots \\ \hline
 & & & \ddots & \ddots
\end{array}\right). \tag{2.26}$$

For practical purposes the Fourier series can be truncated at a finite component with index n_{max}, resulting in a $((2n_{max}+1)\cdot 2)\times((2n_{max}+1)\cdot 2)$ matrix for the eigenvalue

problem, i.e. $(2n_{max}+1)^2$ 2×2 blocks, that can then be treated numerically, for example to find the Floquet-state solutions. For $H_0 = \hbar\nu_F k\sigma_z$, appearing later in this thesis, we can calculate the quasi-energies depending on the momentum k and thereby find a *quasi-band-structure*, that will be an important tool to find appropriate truncation indices for numerical calculations later on.

2.4 2D topological insulators and the BHZ model

The above mentioned tools will be used to investigate the properties of 2D TI edge states. Here we will introduce the model describing them.

2.4.1 Full BHZ Hamiltonian

The model used to describe 2D TIs is the so-called BHZ model introduced in 2006 [7]. The BHZ Hamiltonian was originally developed to investigate HgTe/CdTe quantum wells by considering the band structure of the two materials in a quantum well together with various symmetries. It reads

$$H_{BHZ} = \begin{pmatrix} h\left(\vec{k}\right) & 0 \\ 0 & h^*(-\vec{k}) \end{pmatrix}, \tag{2.27a}$$

$$h\left(\vec{k}\right) = \epsilon\left(\vec{k}\right) + d_i\left(\vec{k}\right)\sigma_i, \tag{2.27b}$$

$$\epsilon\left(\vec{k}\right) = C - D(k_x^2 + k_y^2), \tag{2.27c}$$

$$d_i\left(\vec{k}\right) = \left[Ak_x, -Ak_y, M\left(\vec{k}\right)\right], \tag{2.27d}$$

$$M\left(\vec{k}\right) = M - B(k_x^2 + k_y^2), \tag{2.27e}$$

with A, B, C, D and M being material parameters depending on the specific quantum well geometry [6]. The parameters M and B are commonly called Dirac– and Newton–mass respectively and make up the mass term $M(\vec{k})$, that describes separation between electron and hole bands. It turns out, that the sign relation between M and B determines, whether the system is in a topological state or not. C and D describe the position and shape of the bands considered, where e.g. $C = 0$ and $D = 0$ corresponds to a completely symmetric band structure around the gap center. For us the most important parameter is A since it is associated with the Fermi velocity of the edge states.

This model Hamiltonian can be explicitly solved on an infinite half-plane resulting in two states $\Psi_\uparrow, \Psi_\downarrow$ localized at the edge for certain parameters. [6, 36, 51–53]. The properties of these edge states have been theoretically investigated also for systems other than HgTe/CdTe structures, for example in Bi-thin films confirming the localization at the edge [54]. The two edge states exhibit opposite spin and momentum orientation, so one spin species travels along the edge in one direction, while the other spin species travels in the opposite direction, visualized in Fig. 1.2.

2.4.2 Effective edge Hamiltonian

The Hamiltonian (2.27a) for an infinite half-plane can be projected onto the edge states $\Psi_\uparrow, \Psi_\downarrow$ via $H_{edge}^{\alpha,\beta}(k) = \langle\Psi_\alpha|H_{BHZ}|\Psi_\beta\rangle$. For a symmetric bulk band structure this leads to

the effective edge Hamiltonian [6]

$$H_{edge} = Ak_x\sigma_z = \hbar\nu_F k_x\sigma_z. \tag{2.28}$$

This Hamiltonian now describes the one-dimensional edge of the half-plane and highlights counter-propagating structure of the states. The physical meaning of the only appearing BHZ parameter A as the slope of the edge state dispersion, giving the Fermi velocity, becomes apparent. This effective edge Hamiltonian holds as long as the considered energy lies well within the bulk band gap of the full BHZ Hamiltonian (2.27a). It also has the matrix-structure of a two-level system, motivating the comparison to a driven two-level system later on. Transformation to real space yields the Hamiltonian

$$H_{edge} = -i\hbar\nu_F\partial_x\sigma_z. \tag{2.29}$$

2.4.3 Gap-opening via magnetic fields

The effect of a homogeneous magnetic field on the spectrum and density of states of the effective edge Hamiltonian can explicitly be calculated. If we look at the spectrum of the effective edge Hamiltonian in Eq. (2.28), we find a crossing of the linear dispersion branches at $k = 0$ and no gap. A homogeneous magnetization in the x-y-plane causes a coupling of the two branches via off-diagonal terms in the Hamiltonian and thus the crossing turns into an avoided crossing. This opens a gap in the spectrum, which can be seen in Fig. 2.1 (ungapped in red and gapped in gray), together with the bulk band structure from the full BHZ Hamiltonian (blue). To calculate the density of states for such a case, assume a magnetization, for example in x-direction, i.e. $H = H_{edge} + \Delta\sigma_x$. The eigenvalues of this are determined by

$$0 = \det(H - E) = \det\begin{pmatrix} \hbar\nu_F k - E & \Delta \\ \Delta & \hbar\nu_F k - E \end{pmatrix} = -(\hbar\nu_F k)^2 + E^2 - \Delta^2, \tag{2.30}$$

from which we can calculate the energies as

$$E = \pm\sqrt{\Delta^2 + (\hbar\nu_F k)^2}. \tag{2.31}$$

We see that the band edge lies at $k = 0$, so we expect the gap width in the density of states to be 2Δ. To explicitly calculate the density of states, we start with the equation of motion in momentum space

$$[E - (H_0 + M)]\, G(k, E) = 1 \tag{2.32}$$

which can be formally rearranged to

$$G(k, E) = [E - (H_0 + M)]^{-1}. \tag{2.33}$$

Here, and in all following calculations of this type, we use square brackets to emphasize that $[E - (H_0 + M)]$ is an operator and thus the inversion is not necessarily trivial. Assuming a magnetic field in x-direction we get $M = \Delta\sigma_x$ and we can perform the inversion by expanding with the Pauli-conjugate $E + (H_0 + M)$ leading to

$$G(k, E) = \frac{E + \hbar\nu_F k\sigma_z + \Delta\sigma_x}{E^2 - (\hbar\nu_F k)^2 - \Delta^2}. \tag{2.34}$$

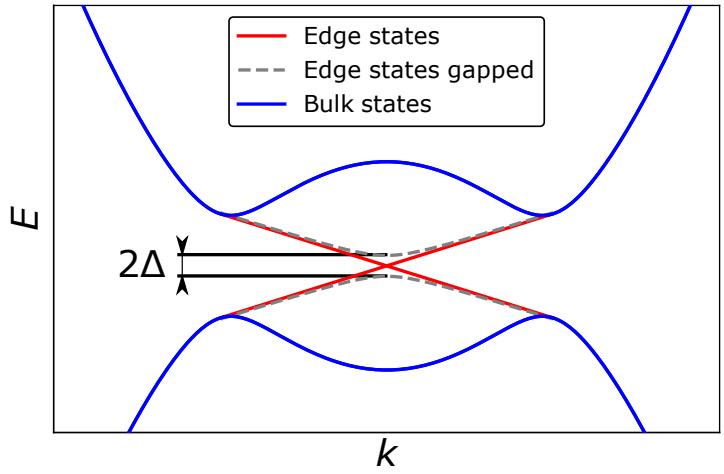

FIG. 2.1: Typical band structure of a 2D TI with the bulk bands (blue) from diagonalizing the full 4×4 BHZ model and the edge states with and without a magnetic field (red and gray respectively) from diagonalizing the effective edge Hamiltonian

The density of states can be found from this via the spectral function

$$\mathcal{D}(E) = -\mathrm{Im}\left(\frac{\mathrm{Tr}\, G(x,x,E)}{\pi}\right). \tag{2.35}$$

The transformation to position space is

$$G(x,x',E) = \int_{-\infty}^{\infty} \frac{\mathrm{d}k}{2\pi} G(k,E) e^{\mathrm{i}k(x-x')} \tag{2.36}$$

and the integration can be performed using the residue theorem, remembering that E carries a small positive imaginary part and carefully keeping track of the pole positions. Detailed calculations can be found in Appendix A.1 and lead to

$$\mathcal{D}(E) = -\mathrm{Im}\left(\frac{\mathrm{Tr}\, G(x,x,E)}{\pi}\right) = \frac{1}{\pi\hbar\nu_F}\frac{|E|}{\sqrt{E^2-\Delta^2}}\,\theta(E^2-\Delta^2) = \frac{1}{\pi\hbar\nu_F} DOS(E). \tag{2.37}$$

Here we can see the density of states for zero magnetization is constant and takes on the value $\frac{1}{\pi\hbar\nu_F}$. In the rest of the thesis we will refer to density of states relative to the constant one for a clean system, denoted by $DOS(E)$. The resulting graph for the density of states is shown in Fig. 2.2(A), where we can clearly see the sharp real gap with edges at $\pm\Delta$ and the approach to a constant non-zero density of states far away from the gap.

2.4.4 Impurity potential and static impurities

Impurities located on the edge channels can be modeled in the edge Hamiltonian Eq. (2.29) as δ-scatterers by

$$H = -i\hbar\nu_F\partial_x\sigma_z + V(x,t) + \vec{M}(x,t)\vec{\sigma}, \tag{2.38a}$$

$$V(x,t) = \sum_l V_l(t)\delta(x-x_l) \tag{2.38b}$$

$$\vec{M}(x,t)\vec{\sigma} = \sum_l \vec{M}_l(t)\vec{\sigma}\delta(x-x_l). \tag{2.38c}$$

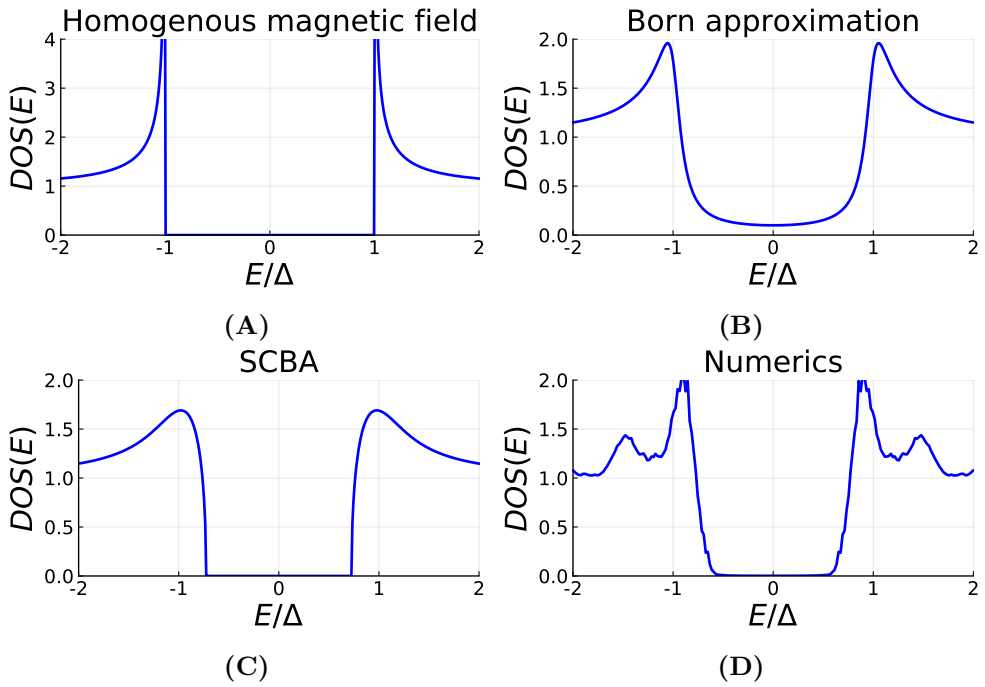

FIG. 2.2: Density of states as a function of energy for (A) a homogeneous magnetic field of strength Δ in x-direction, (B) static impurities using the Born approximation, (C) static impurities using the self-consistent Born approximation and (D) using the numeric model introduced later in the static case. Note the different axis limits for the homogeneous field.

In the general form the l-th impurity has a potential strength of $V_l(t)$ and a magnetic moment of $\vec{M}_l(t)$ that can differ from impurity to impurity. In a previous work [34] we investigated equal, magnetically aligned, static impurities pointing in x-direction, i.e. $V_l(t) = V_0$ and $\vec{M}_l(t) = M_0\vec{e}_x$ for all impurity sites l, that lead to a gap in the density of states. This gap is closed by a rising potential part V_0. The previous work on static impurities used the self-consistent Born-Approximation as well as a numeric impurity averaging approach that is equivalent to the numeric model introduced later, if static impurities are used. Generally, the approaches match very well and show that the influence of the impurities usually leads to a broadening of the dispersion branches, often washing out features that would be sharp if caused by homogeneous fields (compare Fig. 2.2). The mechanism can be seen very well in the Born-approximation as an imaginary part in the self-energy in the Dyson equation leading to the density of states displayed in Fig. 2.2. Another system recently receiving attention is a single non-magnetic but periodically driven impurity, employing Floquet-theory to find the local density of states around the impurity site [31].

In this thesis we investigate equal, randomly placed, magnetically aligned, harmonically rotating impurities with a static potential part. The rotation considered is in the x-z-plane, such that the impurity potentials can be written as $V_l(t) = V_0$ and $\vec{M}_l(t) = M_0(\sin(\Omega t)\vec{e}_x + \cos(\Omega t)\vec{e}_z)$, leading to the Hamiltonian

$$H = -i\hbar\nu_F\partial_x\sigma_z + (V_0 + M_0(\sin(\Omega t)\vec{e}_x + \cos(\Omega t)\vec{e}_z)\vec{\sigma}) \sum_l \delta(x - x_l). \tag{2.39}$$

The system can be visualized as in Fig. 1.3 and the model Hamiltonian Eq. (2.39) will be used frequently to calculate the density of states via the Green's function.

3 Integral equation for the matrix Green's function

In this section a matrix formalism for the Green's function for time-periodic systems is derived and subsequently applied to a simple two-level system. The goal of this formalism is to find the Fourier series of the Green's function. The zeroth component of that Fourier series is then the time-averaged contribution which can be used to find the time averaged density of states via Eq. (2.8). The time-averaged density of states is frequently used to investigate dynamically driven systems [49, 55].

3.1 Matrix Green's function equation

A general time-dependent Hamiltonian can be written in the form

$$H(t) = H_0 + V(t). \tag{3.1}$$

In our case, it will be a time-dependent potential term due to the rotating impurities, but in general it can be any time dependent contribution, e.g. a time-dependent interaction or kinetic energy term. The equation of motion for the Green's function is

$$\left[i\hbar\partial_t - (H_0 + V(t))\right] G(t,t') = \delta(t-t') \tag{3.2}$$

and can be rewritten as an integral equation

$$G(t,t') = g(t-t') + \int \mathrm{d}t_1\, g(t-t_1)V(t_1)G(t_1,t'). \tag{3.3}$$

Here $g(t-t')$ is the Green's function related to H_0 determined by the "free" equation of motion

$$\left[i\hbar\partial_t - H_0\right] g(t-t') = \delta(t-t'). \tag{3.4}$$

For a time-periodic part $V(t+T) = V(t)$ we can use Picard iteration to inductively prove that the Green's function is also time-periodic with period T, i.e. $G(t+T,t'+T) = G(t,t')$. The Picard iteration produces a series according to the recursion relation

$$G^{[n+1]}(t,t') = g(t-t') + \int \mathrm{d}t_1\, g(t-t_1)V(t_1)G^{[n]}(t_1,t), \tag{3.5}$$

with initial value

$$G^{[0]}(t,t') = g(t-t'). \tag{3.6}$$

This series converges for physically relevant cases, essentially the Lipschitz-continuity of the Hamiltonian in G [56]. It can readily be seen that

$$G^{[0]}(t+T,t'+T) = g((t+T)-(t'+T)) = g(t-t') = G^{[0]}(t,t'). \tag{3.7}$$

Using the induction assumption $G^{[n]}(t+T,t'+T) = G^{[n]}(t,t')$ we find

$$\begin{aligned} G^{[n+1]}(t+T,t'+T) &= g(t-t') + \int \mathrm{d}t_1\, g(t+T-t_1)V(t_1)G^{[n]}(t_1,t'+T) \\ &= g(t-t') + \int \mathrm{d}t_1\, g(t+T-t_1)V(t_1)G^{[n]}(t_1-T,t'), \end{aligned} \tag{3.8}$$

and with the change of variables $t_1 - T \to t_1$ and the periodicity of $V(t)$ it follows that

$$\begin{aligned} G^{[n+1]}(t+T, t'+T) &= g(t-t') + \int \mathrm{d}t_1\, g(t-t_1) V(t_1+T) G^{[n]}(t_1, t') \\ &= g(t-t') + \int \mathrm{d}t_1\, g(t-t_1) V(t_1) G^{[n]}(t_1, t') \\ &\equiv G^{[n+1]}(t, t'). \end{aligned} \tag{3.9}$$

By induction this proves the time-periodicity. We can now define the Fourier transform with respect to t' as

$$\tilde{G}(t, E) = \int \mathrm{d}\tau\, e^{i\frac{E}{\hbar}\tau} G(t, t-\tau). \tag{3.10}$$

Analogously to the proof before it can be shown that $\tilde{G}(t, E)$ is also time-periodic, i.e. $\tilde{G}(t+T, E) = \tilde{G}(t, E)$. The time-periodicity now allows us to write the Green's function as a Fourier series

$$\tilde{G}(t, E) = \sum_{n \in \mathbb{Z}} e^{in\frac{2\pi}{T}t} \tilde{G}_n(E), \tag{3.11}$$

where the Fourier components $\tilde{G}_n(E)$ are defined according to

$$\tilde{G}_n(E) = \frac{1}{T} \int_0^T \mathrm{d}t\, e^{-\mathrm{i}n\frac{2\pi}{T}t} \tilde{G}(t, E). \tag{3.12}$$

Applying Eq. (3.10) to the integral Eq. (3.3) after some calculation gives

$$\tilde{G}(t, E) = \tilde{g}(E) + \int \mathrm{d}\tau_1\, e^{i\frac{E}{\hbar}\tau_1} g(\tau_1) V(t-\tau_1) \tilde{G}(t-\tau_1, E), \tag{3.13}$$

where $\tilde{g}(E)$ is the Fourier transform of $g(t-t')$ according to Eq. (3.10). This in turn can be used to calculate the Fourier coefficients

$$\begin{aligned} \tilde{G}_n(E) &= \tilde{g}(E)\delta_{n,0} \\ &\quad + \frac{1}{T} \int_0^T \mathrm{d}t\, e^{-in\frac{2\pi}{T}t} \int \mathrm{d}\tau_1\, e^{i\frac{E}{\hbar}\tau_1} g(\tau_1) V(t-\tau_1) \tilde{G}(t-\tau_1, E) \\ &= \tilde{g}(E)\delta_{n,0} \\ &\quad + \sum_{n_1, n_2} \int \mathrm{d}\tau_1\, e^{i\frac{E}{\hbar}\tau_1} g(\tau_1) V_{n_1} \tilde{G}_{n_2}(E) e^{-i(n_1+n_2)\frac{2\pi}{T}\tau_1} \delta_{n, n_1+n_2}, \end{aligned} \tag{3.14}$$

where the Fourier series according to (3.11) for $V(t)$ and $\tilde{G}(t, E)$ have been inserted. The Kronecker delta δ_{n,n_1+n_2} is introduced by the t-integral

$$\frac{1}{T} \int_0^T \mathrm{d}t\, e^{i(n_1+n_2-n)\frac{2\pi}{T}t} = \delta_{n,n_1+n_2}. \tag{3.15}$$

Performing the sum and collecting the exponentials leads to

$$\begin{aligned} \tilde{G}_n(E) &= \tilde{g}(E)\delta_{n,0} + \sum_{n_1} \int \mathrm{d}\tau_1\, e^{i\frac{E}{\hbar}\tau_1} g(\tau_1) V_{n_1} \tilde{G}_{n-n_1}(E) e^{-in\frac{2\pi}{T}\tau_1} \\ &= \tilde{g}(E)\delta_{n,0} + \sum_{n_1} \int \mathrm{d}\tau_1\, e^{i\frac{1}{\hbar}(E-n\hbar\Omega)\tau_1} g(\tau_1) V_{n_1} \tilde{G}_{n-n_1}(E) \\ &= \tilde{g}(E)\delta_{n,0} + \tilde{g}(E - n\hbar\Omega) \sum_m V_m \tilde{G}_{n-m}(E). \end{aligned} \tag{3.16}$$

This set of coupled equations is fairly general and holds for time-periodic potentials, as long as the Picard-series converges.

For static potentials, i.e. $V(t) = const.$, all but the zeroth Fourier component of V vanish and the equations decouple to

$$\tilde{G}_0(E) = \tilde{g}(E) + \tilde{g}(E)V_0\tilde{G}_0(E) \tag{3.17a}$$

$$\tilde{G}_n(E) = 0, \quad n \neq 0. \tag{3.17b}$$

The Green's function is then also time-independent and this approach also includes the static impurities case discussed in Ref. [34].

For harmonic driving we get

$$V(t) = V_0 + V_+ e^{i\Omega t} + V_+^\dagger e^{-i\Omega t} \tag{3.18}$$

resulting in

$$\begin{aligned}\tilde{G}_n(E) = \tilde{g}(E)\delta_{n,0} &+ \tilde{g}(E - n\hbar\Omega)V_0\tilde{G}_n(E) \\ &+ \tilde{g}(E - n\hbar\Omega)V_+\tilde{G}_{n-1}(E) \\ &+ \tilde{g}(E - n\hbar\Omega)V_+^\dagger\tilde{G}_{n+1}(E).\end{aligned} \tag{3.19}$$

This can be rearranged to

$$\begin{aligned}\tilde{g}(E)\delta_{n,0} = (1 - \tilde{g}(E - n\hbar\Omega)V_0)&\tilde{G}_n(E) \\ - \tilde{g}(E - n\hbar\Omega)V_+&\tilde{G}_{n-1}(E) \\ - \tilde{g}(E - n\hbar\Omega)V_+^\dagger&\tilde{G}_{n+1}(E),\end{aligned} \tag{3.20}$$

which highlights the matrix form of this equation

$$\begin{pmatrix} \ddots & \ddots & & & \\ \ddots & 1 - \tilde{g}(E + \hbar\Omega)V_0 & -\tilde{g}(E + \hbar\Omega)V_+^\dagger & & \\ & -\tilde{g}(E)V_+ & 1 - \tilde{g}(E)V_0 & -\tilde{g}(E)V_+^\dagger & \\ & & -\tilde{g}(E - \hbar\Omega)V_+ & 1 - \tilde{g}(E - \hbar\Omega)V_0 & \ddots \\ & & & \ddots & \ddots \end{pmatrix} \begin{pmatrix} \vdots \\ \tilde{G}_{-1}(E) \\ \tilde{G}_0(E) \\ \tilde{G}_1(E) \\ \vdots \end{pmatrix} = \begin{pmatrix} \vdots \\ 0 \\ \tilde{g}(E) \\ 0 \\ \vdots \end{pmatrix}. \tag{3.21}$$

This resembles the block-tri-diagonal structure of a Floquet-matrix. In principle, higher Fourier components of the driving term $V(t)$ will cause further off-diagonals to appear which could be included to look at non-harmonic driving, but at a numerical cost. The time-independent part of the Green's function is then simply the zeroth Fourier component $\tilde{G}_0(E)$ and can be used to access the time-averaged quantities derived from the Green's function.

3.2 Application to a driven two-level system

The matrix Eq. (3.16) is very general and holds for many systems. In particular, the necessary assumptions are the existence of the Fourier series of the periodic potential and the convergence of the Picard series. Generally, solving this equation can become very difficult, but for some cases it can readily be solved. We will now show that the explicit

solution to a simple example system also solves the matrix Eq. (3.16). The example system will be a diagonally driven two-level system described by the Hamiltonian

$$H = k\sigma_z + V\sigma_z \sin \Omega t. \tag{3.22}$$

This corresponds to the effective edge Hamiltonian in the BHZ model with a driven homogeneous magnetic field in z-direction. The exact solutions for the Fourier components of the Greens function for this system are

$$\tilde{G}_n(E) = \mathrm{i}^n \sum_l J_{n-l}\left(\frac{V\sigma_z}{\hbar\Omega}\right) J_l\left(-\frac{V\sigma_z}{\hbar\Omega}\right) \tilde{g}(E - l\hbar\Omega), \tag{3.23}$$

where the J_n are Bessel functions of the first kind and applied to the Pauli-z-matrices have to be understood as

$$J_k\left(\frac{V\sigma_z}{\hbar\Omega}\right) = \begin{pmatrix} J_k\left(\frac{V}{\hbar\Omega}\right) & 0 \\ 0 & J_k\left(-\frac{V}{\hbar\Omega}\right) \end{pmatrix}. \tag{3.24}$$

The calculations can be found in Appendix B. We will show that the explicit solution Eq. (3.23) is equivalent to the matrix equation (3.16) from the integral Green's function approach.

For a periodic potential $V(t) = V\sigma_z \sin \Omega t = \frac{V\sigma_z}{2\mathrm{i}}(e^{\mathrm{i}\Omega t} - e^{-\mathrm{i}\Omega t})$ the matrix Eq. (3.16) reduces to

$$\begin{aligned} \tilde{G}_n(E) = \tilde{g}(E)\delta_{n,0} &+ \tilde{g}(E - n\hbar\Omega)\left(\frac{V\sigma_z}{2\mathrm{i}}\right)\tilde{G}_{n-1}(E) \\ &+ \tilde{g}(E - n\hbar\Omega)\left(-\frac{V\sigma_z}{2\mathrm{i}}\right)\tilde{G}_{n+1}(E) \end{aligned} \tag{3.25}$$

We start with Eq. (3.23) by adding a 0 and introducing a factor of 1 to get

$$\tilde{G}_n(E) = \underbrace{\tilde{g}(E)\delta_{n,0} - \tilde{g}(E)\delta_{n,0}}_{=0} + \underbrace{\tilde{g}(E - n\hbar\Omega)\tilde{g}(E - n\hbar\Omega)^{-1}}_{=1}\tilde{G}_n(E). \tag{3.26}$$

Noting that $\tilde{g}(E)\delta_{n,0} = \tilde{g}(E - n\hbar\Omega)\delta_{n,0}$ and $\tilde{g}(E - n\hbar\Omega)^{-1} = E - n\hbar\Omega - k\sigma_z = \tilde{g}(E)^{-1} - n\hbar\Omega$, we can write

$$\tilde{G}_n(E) = \tilde{g}(E)\delta_{n,0} - \tilde{g}(E - n\hbar\Omega)\underbrace{\left[\delta_{n,0} - (\tilde{g}(E)^{-1} - n\hbar\Omega)\tilde{G}_n(E)\right]}_{(*)}. \tag{3.27}$$

To rewrite the last part $(*)$ we note that

$$\delta_{n,0} = \mathrm{i}^n\delta_{n,0} = \mathrm{i}^n J_n(0) = \mathrm{i}^n J_n(\tilde{V} - \tilde{V}) = \mathrm{i}^n \sum_l J_{n-l}(\tilde{V})J_l(-\tilde{V}), \tag{3.28}$$

where we used *Neumann*s addition theorem for Bessel functions in the last step. This has the same form as the sum in Eq. (3.23) and allows us to write $(*)$ as

$$(*) = \mathrm{i}^n \sum_l J_{n-l}(\tilde{V})J_l(-\tilde{V})\left[\underbrace{1 - \tilde{g}(E)^{-1}\tilde{g}(E - l\hbar\Omega)}_{(**)} + n\hbar\Omega\tilde{g}(E - l\hbar\Omega)\right]. \tag{3.29}$$

We can calculate $(**)$ to be

$$\begin{aligned} 1-\tilde{g}(E)^{-1}\tilde{g}(E-l\hbar\Omega) &= \frac{E-l\hbar\Omega-k\sigma_z}{E-l\hbar\Omega-k\sigma_z} - \frac{(E-k\sigma_z)}{E-l\hbar\Omega-k\sigma_z} \\ &= \frac{E-l\hbar\Omega-k\sigma_z-(E-k\sigma_z)}{E-l\hbar\Omega-k\sigma_z} \\ &= (-l\hbar\Omega)\tilde{g}(E-l\hbar\Omega). \end{aligned} \tag{3.30}$$

These calculations can also be done going back to the integral representation of $\tilde{g}(E)$ in terms of the formal solution $g(\tau)$ and using integration by parts. Inserting back into $(*)$ leads to

$$\begin{aligned} (*) &= \mathrm{i}^n \sum_l J_{n-l}(\tilde{V})J_l(-\tilde{V})\left[(-l\hbar\Omega)\tilde{g}(E-l\hbar\omega)+n\hbar\Omega\tilde{g}(E-l\hbar\Omega)\right] \\ &= \mathrm{i}^n \sum_l (n-l)\hbar\Omega J_{n-l}(\tilde{V})J_l(-\tilde{V})\tilde{g}(E-l\hbar\Omega) \\ &= \mathrm{i}^n \sum_l \frac{V\sigma_z}{2}\frac{2(n-l)}{\tilde{V}}\hbar\Omega J_{n-l}(\tilde{V})J_l(-\tilde{V})\tilde{g}(E-l\hbar\Omega). \end{aligned} \tag{3.31}$$

We can now apply the recursion relation $\frac{2k}{x}J_n(x) = J_{n-1}(x)+J_{n+1}(x)$ to get

$$\begin{aligned} (*) &= \mathrm{i}^n \sum_l \frac{V\sigma_z}{2}(J_{n-1-l}(\tilde{V})+J_{n+1-l}(\tilde{V}))J_l(-\tilde{V})\tilde{g}(E-l\hbar\Omega) \\ &= -\frac{V\sigma_z}{2\mathrm{i}}\mathrm{i}^{n-1}\sum_l J_{n-1-l}\left(\frac{V\sigma_z}{\hbar\Omega}\right)J_l\left(-\frac{V\sigma_z}{\hbar\Omega}\right)\tilde{g}(E-l\hbar\Omega) \\ &\quad + \frac{V\sigma_z}{2\mathrm{i}}\mathrm{i}^{n+1}\sum_l J_{n+1-l}\left(\frac{V\sigma_z}{\hbar\Omega}\right)J_l\left(-\frac{V\sigma_z}{\hbar\Omega}\right)\tilde{g}(E-l\hbar\Omega) \\ &= -\frac{V\sigma_z}{2\mathrm{i}}\tilde{G}_{n-1}(E)+\frac{V\sigma_z}{2\mathrm{i}}\tilde{G}_{n+1}(E). \end{aligned} \tag{3.32}$$

Inserting this in Eq. (3.27) we arrive at

$$\begin{aligned} \tilde{G}_n(E) = \tilde{g}(E)\delta_{n,0} &+ \tilde{g}(E-n\hbar\Omega)\left(\frac{V\sigma_z}{2\mathrm{i}}\right)\tilde{G}_{n-1}(E) \\ &+ \tilde{g}(E-n\hbar\Omega)\left(-\frac{V\sigma_z}{2\mathrm{i}}\right)\tilde{G}_{n+1}(E), \end{aligned} \tag{3.33}$$

which is precisely Eq. (3.25). This confirms that the Matrix Green's function approach produces exact results for this case. For the numerical implementation one has to approximate the Fourier components and truncate the series at an appropriate place to get finite-dimensional matrices.

4 Application to the impurity edge system

To apply the matrix Eq. (3.21) from the previous section, we need to write our system in a particular form. In this section we will derive this specific form for an effective edge impurity system and introduce scaling and cut-off parameters to obtain useful, finite dimensional matrices before we will introduce a basic impurity averaging method.

4.1 Impurity Green's function and dynamic potential

In this section we will derive an equation for the real space Green's function of the effective edge Hamiltonian with impurities having a static potential part and dynamic magnetic moment. This will be done in such way that we can directly apply the matrix Eq. (3.21). Additionally, we calculate the needed transformation from time to energy domain.

4.1.1 Real-space integral equation

In its most general form the edge Hamiltonian looks like

$$H = -i\hbar\nu_F\partial_x\sigma_z + V(x) + \vec{M}(x,t)\vec{\sigma}, \tag{4.1}$$

providing the equation of motion

$$\left[-i\hbar\partial_t + i\hbar\nu_F\partial_x\sigma_z - V(x) - \vec{M}(x,t)\vec{\sigma}\right] G(x,x',t,t') = \delta(x-x')\delta(t-t'). \tag{4.2}$$

The diagonal, static contribution $V(x)$ can be treated exactly. Introducing a unitary matrix

$$U_V(x,x') = e^{i\frac{\sigma_z}{\hbar\nu_F}\left(\int_{-\infty}^{x}\mathrm{d}y\,V(y) - \int_{-\infty}^{x'}\mathrm{d}y\,V(y)\right)}, \tag{4.3}$$

the Green's function can be rewritten as

$$G(x,x',t,t') = U_V(x,x')\tilde{G}(x,x',t,t'). \tag{4.4}$$

Inserting this into Eq. (4.2) and multiplying by $U_V^\dagger(x,x')$ from the left provides

$$\left[-i\hbar\partial_t + i\hbar\nu_F\sigma_z\partial_x - U_V^\dagger(x,x')\vec{M}(x,t)\vec{\sigma}U_V(x,x')\right]\tilde{G}(x,x',t,t') = \delta(x-x')\delta(t-t') \tag{4.5}$$

and with the free Green's function $g_0(x-x',t-t')$, defined by

$$\left[-i\hbar\partial_t + i\hbar\nu_F\partial_x\sigma_z\right] g_0(x-x',t-t') = \delta(x-x')\delta(t-t'), \tag{4.6}$$

we can write this as the integral equation

$$\begin{aligned}\tilde{G}(x,x',t,t') = {} & g_0(x-x',t-t') \\ & + \int\int \mathrm{d}x_1\ \mathrm{d}t_1\, g_0(x-x_1,t-t_1) \\ & \times U_V^\dagger(x_1,x')\vec{M}(x_1,t_1)\vec{\sigma}U_V(x_1,x')\tilde{G}(x_1,x',t_1,t').\end{aligned} \tag{4.7}$$

This is an integral equation for $\tilde{G}(x,x',t,t')$ and the corresponding integral equation for $G(x,x',t,t')$ can be found by multiplying with $U_V(x,x')$ from the and applying Eq. (4.4). The result is

$$\begin{aligned} G(x,x',t,t') = g(x,x',t-t') \\ + \int\int \mathrm{d}x_1 \; \mathrm{d}t_1 \, U_V(x,x') g_0(x-x_1,t-t_1) \\ \times U_V^\dagger(x_1,x') \vec{M}(x_1,t_1) \vec{\sigma} G(x_1,x',t_1,t'). \end{aligned} \tag{4.8}$$

Here we used the corresponding definition of Eq. (4.4) for g_0. This can be further simplified by noticing that U_V and g_0 are diagonal matrices and therefore commute. We can calculate

$$\begin{aligned} U_V(x,x') g_0(x-x_1,t-t_1) U_V^\dagger(x_1,x') &= U_V(x,x') U_V^\dagger(x_1,x') g_0(x-x_1,t-t_1) \\ &= U_V(x,x_1) g_0(x-x_1,t-t_1) \\ &= g(x,x_1,t-t_1) \end{aligned} \tag{4.9}$$

and write Eq. (4.8) as

$$\begin{aligned} G(x,x',t,t') = g(x,x',t-t') \\ + \int\int \mathrm{d}x_1 \; \mathrm{d}t_1 \, g(x,x_1,t-t_1) \vec{M}(x_1,t_1) \vec{\sigma} G(x_1,x',t_1,t'). \end{aligned} \tag{4.10}$$

Note that up to this point no further assumptions on the form of $V(x)$ and $\vec{M}(x,t)\vec{\sigma}$ have been made. The calculations have shown, that in principle a static magnetic part in z-direction can be absorbed into the free Green's function $g(x,x',t-t')$ as an overall phase factor, but at the cost of losing the overall translational invariance of the *free* Green's function g. The practical limitations are then, that $V(x)$ is t-independent and that the integral in the exponent in Eq. (4.3) can be solved. Whether or not that is viable is a separate consideration.The main concern for the next step is the form of the magnetic contribution $\vec{M}(x,t)\vec{\sigma}$.

4.1.2 Dynamic impurity matrix Green's function

We now want to introduce the impurity nature of the perturbation by setting

$$\vec{M}(x,t)\vec{\sigma} = \sum_l \vec{M}_l(t) \vec{\sigma} \delta(x-x_l). \tag{4.11}$$

This enables us to evaluate the x-integral in Eq. (4.10) and write

$$G(x,x',t,t') = g(x,x',t-t') + \sum_l \int \mathrm{d}t_1 \, g(x,x_l,t-t_1) \vec{M}_l(t_1) \vec{\sigma} G(x_l,x',t_1,t'). \tag{4.12}$$

By evaluating this equation at the impurity positions we can write

$$\begin{aligned} G(x_m,x_n,t,t') &= g(x_m,x_n,t-t') \\ &\quad + \sum_l \int \mathrm{d}t_1 \, g(x_m,x_l,t-t_1) \vec{M}_l(t_1) \vec{\sigma} G(x_l,x_n,t_1,t') \\ &= g(x_m,x_n,t-t') \\ &\quad + \sum_l \sum_k \int \mathrm{d}t_1 \, g(x_m,x_l,t-t_1) (\vec{M}_l(t_1) \vec{\sigma} \delta_{l,k}) G(x_k,x_n,t_1,t'), \end{aligned} \tag{4.13}$$

where we introduced an additional sum over a Kronecker-delta in the last step. By defining the matrix notation

$$[G(t,t')]_{m,n} = G(x_m, x_n, t, t'), \tag{4.14a}$$
$$[g(t-t')]_{m,n} = g(x_m, x_n, t-t'), \tag{4.14b}$$
$$[M(t)]_{m,n} = (\vec{M}_m(t)\vec{\sigma})\delta_{m,n}, \tag{4.14c}$$

we can write the integral equation in full matrix form as

$$G(t,t') = g(t-t') + \int \mathrm{d}t_1\, g(t-t_1)M(t_1)G(t_1,t') \tag{4.15}$$

which has precisely the form of Eq. (3.3), such that we can apply the formalism constructed in section 3 and solve the corresponding matrix Eq. (3.16) to find the Green's function for the dynamic impurity problem.

Note that the matrix form with the impurity indices is enabled by the delta-shape of the impurities, not the form of $\vec{M}_l(t)\vec{\sigma}$, thus it is in principle also possible to treat dynamic potential parts by adapting the matrix $M(t)$. Similarly static diagonal contributions can be incorporated in $g(t-t')$. In this form we can also see, that information about the impurity positions in the equation for $G(t,t')$ is contained in $g(t-t')$, while information about the impurities themselves, i.e. strength of the individual δ-impurities, is contained in $M(t)$.

4.1.3 Transformation to energy domain

To apply the matrix Eq. (3.21) we now have to calculate the potential impurity Green's function in Energy domain $\tilde{g}(E)$. It is the Fourier transform of $g(t-t')$ and can be calculated block-wise via the free Green's function and the unitary $U_V(x,x')$ according to Eq. (4.4). The free real-space Green's function in Energy domain is also used for the static impurity case [34] and reads

$$\begin{aligned} g_0(x-x',E) = \frac{-i}{2\hbar\nu_F}\Bigg[& e^{\frac{E(x-x')}{\hbar\nu_F}}\theta(x-x')(1+\sigma_z) \\ & + e^{-\frac{E(x-x')}{\hbar\nu_F}}(1-\theta(x-x'))(1-\sigma_z)\Bigg]. \end{aligned} \tag{4.16}$$

The calculations can be found in Appendix A.2. We can also evaluate the integral in the exponential in $U_V(x,x')$ if we insert the potential part of the impurities

$$V(x) = \sum_l V_l \delta(x-x_l). \tag{4.17}$$

and find

$$U_V(x,x') = e^{i\frac{\sigma_z}{\hbar\nu_F}\sum_l V_l(\theta(x-x_l)-\theta(x'-x_l))}. \tag{4.18}$$

Evaluation at the impurity positions, remembering to treat the Heaviside functions in a weak sense, i.e. $\lim_{x\to 0}\theta(x) = 1/2$, then gives the blocks of $\tilde{g}(E)$.

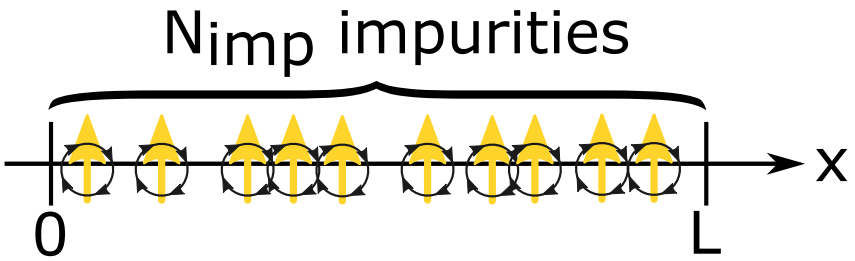

FIG. 4.1: N_{imp} rotating impurities (yellow arrows) in a finite interval $(0, L)$

4.1.4 Fourier decomposition of the potential matrix

This far we have not specified the exact form of $\vec{M}_l(t)\vec{\sigma}$. The formalism allows for any time-periodic function here, but we are interested in a particularly easy case, namely harmonically driven, equal impurities rotating in the x-z-plane. That means, we assume $\vec{M}_l(t) = M_0(\sin(\Omega t), 0, \cos(\Omega t))$ for all l. Writing the sin / cos-functions as complex exponentials we can then calculate

$$\vec{M}_l(t)\vec{\sigma} = M_0(\sin(\Omega t)\vec{e}_x + \cos(\Omega t)\vec{e}_z)\vec{\sigma} = \frac{M_0}{2i}(\sigma_x + i\sigma_z)e^{i\Omega t} - \frac{M_0}{2i}(\sigma_x - i\sigma_z)e^{-i\Omega t}. \quad (4.19)$$

In this form we can immediately identify the diagonal blocks of V_+ to be $\frac{M_0}{2i}(\sigma_x + i\sigma_z)$ and we have found all parts we need to calculate the full Green's function.

4.2 Parameters and scaling

For the numerical implementation we want to write the input parameters in appropriate units. Similarly, we have to take a look at the numerical parameters in order to have a finite dimensional problem and still find physically relevant results.

If we look at an impurity system with N_{imp} static impurities placed in an interval $(0, L)$, i.e. $M(x) = \sum_{l=1}^{N_{imp}} M\delta(x - x_l)$ where $x_l \in (0, L)$ (compare Fig. 4.1, for details on projecting the 3D impurity distribution onto the edge state see Ref [34]), we can write the average magnetization Δ as

$$\Delta = \frac{1}{L}\int_0^L M(x)\,\mathrm{d}x = \sum_{l=1}^{N_{imp}} M\frac{1}{L}\underbrace{\int_0^L \delta(x - x_l)\,\mathrm{d}x}_{=1} = \frac{N_{imp}}{L}M = nM \quad (4.20)$$

with the impurity density $n = \frac{N_{imp}}{L}$. Here we can interpret the interval with the static impurities as a barrier with an average magnetization Δ, i.e. $H(x) = \hbar\nu_F k\sigma_z + \Delta\sigma_x(\theta(x)\theta(L - x))$. Assuming $x_l \neq x_k$ for any two impurities l and k, the continuous limit $n \to \infty$ while $\Delta = nM = const.$ results in precisely this Hamiltonian. This justifies the interpretation as a barrier. From the calculations in section 2.4.3 we know that a homogeneous magnetization Δ in x-direction opens a gap with edges at $E = \pm\Delta$. This motivates measuring the energy in terms of this gap size Δ.

In the barrier picture we can also solve the stationary Schrödinger equation explicitly. Outside the barrier the two components decouple and we get counter-propagating free waves $\propto \exp(\pm \mathrm{i}E/(\hbar\nu_F)x)$ in the upper/lower component. Inside the magnetic barrier the Schrödinger equation reads (suppressing the arguments of the wave function)

$$(-i\hbar\nu_F\sigma_z\partial_x + \Delta\sigma_x)\Psi = E\Psi. \quad (4.21)$$

This can be written as a set of coupled ordinary differential equations

$$\partial_x \Psi_1 = \mathrm{i}\tilde{E}\Psi_1 - \mathrm{i}\tilde{\Delta}\Psi_2 \tag{4.22a}$$

$$-\partial_x \Psi_2 = \mathrm{i}\tilde{E}\Psi_2 - \mathrm{i}\tilde{\Delta}\Psi_1, \tag{4.22b}$$

where $\tilde{E} = {}^{E}/_{\hbar\nu_F}$ and $\tilde{\Delta} = {}^{\Delta}/_{\hbar\nu_F}$. For $x < 0$ and $x > L$ (outside the barrier) these decouple and give the plane wave solutions mentioned earlier. Eq. (4.22a) can be rewritten as

$$\Psi_2 = \frac{\mathrm{i}}{\tilde{\Delta}}\partial_x \Psi_1 + \frac{\tilde{E}}{\tilde{\Delta}}\Psi_1 \tag{4.23}$$

and inserted into Eq. (4.22b). The first derivatives cancel out and multiplying by $\mathrm{i}\tilde{\Delta}$ leads to

$$\partial_x^2 \Psi_1 = (\tilde{\Delta}^2 - \tilde{E}^2)\Psi_1. \tag{4.24}$$

The same equation is found in a similar manner for Ψ_2. This shows that the wave equations will be super-positions of $\exp(\pm\sqrt{\tilde{\Delta}^2 - \tilde{E}^2}x)$. The exact form can be found demanding continuity at the barriers edges. We will find an exponential decay into the barrier with a decay length (at $E = 0$) of $l_\Delta = 1/\tilde{\Delta} = {}^{\hbar\nu_F}/_{\Delta}$. An important thing to notice is that due to the E-dependence of the decay length we will not get sharp edge boundaries, since for energies close to the gap edge we will get tunneling and there will be states penetrating the gap.

The decay length can be related to the impurity strength via $\Delta = nM$ and $\tilde{\Delta} = {}^{\Delta}/_{\hbar\nu_F}$ which motivates giving M in units of $\hbar\nu_F$. Furthermore, we can relate the impurity strength to the size of the system via the impurity density like

$$l_\Delta = \frac{1}{n\frac{M}{\hbar\nu_F}} = \frac{1}{\frac{N_{imp}}{L}\frac{M}{\hbar\nu_F}}$$

$$\Rightarrow \frac{L}{l_\Delta} = N_{imp}\frac{M}{\hbar\nu_F}. \tag{4.25}$$

By choosing ${}^{L}/_{l_\Delta}$ to be big enough, so we do not get significant tunneling through the barrier (say ${}^{L}/_{l_\Delta} = 6 \to 8$), and choosing the impurity strength we can calculate the number of impurities in the system needed to avoid significant tunneling. Additionally, we have to ensure that we have enough impurities to be able to see multi-impurity effects.

The last physical parameter that has to be considered is the driving frequency Ω. There are two separate approaches that lead to the same conclusion. Firstly, we can consider the response time of the system with regards to a change from a gapped to an ungapped state. This will be done in a later section. Alternatively, we can simply notice that in the matrix Eq. (3.21) $\hbar\Omega$ will always appear in the argument of the free Green's function added to the energy E. Thus, giving $\hbar\Omega$ on the same scale as E is the natural choice.

In summary our input parameters for the numerical model will be ${}^{M}/_{\hbar\nu_F}$ for the magnetic strength, ${}^{V}/_{M}$ for the potential strength, ${}^{E}/_{\Delta}$ for the energy and ${}^{\hbar\Omega}/_{\Delta}$ for the driving frequency. Additionally, we introduced the parameter ${}^{L}/_{l_\Delta}$ that controls the system length and determines the number of impurities via 4.25.

The numerical parameters are the number of Fourier components determined by the biggest Fourier index n_{max}, and the number of impurity averaging runs n_{runs}, that will be discussed separately in the following chapters.

4.2.1 Realistic parameters

While the numerical parameters will be given by practical considerations, the physical parameters can be chosen somewhat freely. In our previous work Ref. [34] for static impurities the connection between 3D impurities in a realistic system and the effective 1D impurity strength has been drawn. This was done by projecting δ-impurities in a 3D system onto the edge states. The results translate to $0.02 < {}^{M}/_{\hbar\nu_F} < 0.4$ as a realistic range for the magnetic impurity strength.

In realistic systems finite size effects that open a gap by coupling opposing edges need to be taken into account [36, 57]. Since we are using an effective single edge model, starting out from an infinite half-plane with only one edge, these effects are excluded from our calculations and do not need to be considered.

For numerical reasons, however, we need to avoid impurities being placed too closely together. We can manually place a lower bound on the impurity distance when creating random impurity distributions. If we choose the minimal distance to be $\Delta_{imps} = 10^{-6}L$ we can calculate

$$\Delta_{imps} = 10^{-6} = 10^{-6} \cdot 8l_{\Delta} = 8 \cdot 10^{-6}\frac{1}{nM} \tag{4.26}$$

Typically, we will have values of ${}^{M}/_{\hbar\nu_F} = 0.2$ and 3D doping densities of $n_{3D} \approx 10^{13} - 10^{17}\,{}^{1}/_{\mathrm{cm}}$ [4] which translates to a 1D doping density of $n_{1D} = \sqrt[3]{n_{3D}} \approx 10^{4} - 10^{6}\,{}^{1}/_{\mathrm{cm}}$. Inserting this leaves us with $\Delta_{imps} \approx 10^{-2} - 10^{-4}\,{}^{1}/_{\mathrm{nm}}$, so the minimal impurity distance is approximately in the Å-range. Considering the lattice constant in HgTe and InAs is approximately 0.6Å, this minimal impurity distance is a reasonable choice.

4.3 Fourier component estimates

In addition to a finite number of impurities, to end up with a finite dimensional matrix equation that can then be solved numerically the Fourier series for $G(t, E)$ has to be truncated. Finding suitable truncation indices can be approached in two different pictures and here we will discuss these approaches to find reasonable truncation indices for the Fourier series for different driving regimes.

System response time If we look at the energy range around the gap, we can look at the dynamics in a static gapped and a static ungapped system , i.e. impurities aligned in x/z–direction respectively. In both cases the system can be diagonalized and we can write the time evolution operator as

$$U(t) = \exp\left(\begin{pmatrix} i\frac{E_+}{\hbar}t & 0 \\ 0 & i\frac{E_-}{\hbar}t \end{pmatrix}\right), \tag{4.27}$$

where $E_\pm$ are the respective eigen-energies of the system. For the gapped system they are $E_\pm = \pm\sqrt{\Delta^2 + (\hbar\nu_F k)^2}$ and for the ungapped system $E_\pm = \pm(\Delta + \hbar\nu_F k)$. Since we are using the effective edge Hamiltonian, we consider momenta k well within the bulk band edges and as a rough estimate for the fastest dynamics ${}^{2\Delta}/_{\hbar}$ shall suffice. That means, in the dynamic system around the band gap no effects faster than this should occur and Fourier components with frequencies higher than ${}^{2\Delta}/_{\hbar}$ will be sufficiently small. Since the Fourier decomposition is performed in terms of the driving frequency Ω, we can require ${}^{2\Delta}/_{\hbar\Omega} \lesssim n_{max}$ for the cut-off. Here we can again see that scaling $\hbar\Omega$ similar to the Energy is the most natural way for a reasonable scaling.

Band structure Alternatively, we can look at the quasi-energy band structure given by the eigenvalues E_n of the Floquet Hamiltonian. The Floquet Hamiltonian can be calculated similarly to section 2.3.1. Consider a homogeneous rotating magnetic field, i.e. a Hamiltonian $H = H_0 + \Delta(\sin(\Omega t)\sigma_x + \cos(\Omega t)\sigma_z)$. In momentum domain the Hamiltonian reads $H_0(k) = \hbar\nu_F k\sigma_z$ and we have a two-level system for a fixed value of k. Similar to section 2.3.1, we can use the Floquet Hamiltonian and, after truncating, calculate the eigenvalues to find a quasi-band structure. Firstly, note that the quasi energies follow the rule $E_n = E_0 - n\hbar\Omega$, so every Fourier component corresponds to a quasi energy in the band structure that is shifted by $\pm\hbar\Omega$. The off-diagonal blocks in the Floquet Hamiltonian introduce a coupling between these branches. If the Fourier series is truncated at n_{max}, higher bands and the coupling to them is not considered. This can be seen by a violation of the periodicity condition $E_n = E_0 - n\hbar\Omega$ and means that to get reasonable results we need to make sure we carry enough Fourier components such that the quasi-energies in the desired energy range are periodic. The periodicity of the quasi-energies indicates whether the cut-off for the Fourier series was large enough. Naturally, this means that the cut-off will also be determined by the energy range in which the density of states is to be calculated.

Alternatively to calculating the band structure directly, we can use the matrix Eq. (3.21) and truncate it to calculate $G_0(k, E)$ explicitly. For $n_{max} = 2$ this gives

$$\begin{aligned} G_0(k,E) = \Bigg(1 - \tilde{g}(k,E)\Bigg[V_+ \frac{\tilde{g}(k,E+\hbar\Omega)}{1-\tilde{g}(k,E+\hbar\Omega)V_+\tilde{g}(k,E+2\hbar\Omega)V_+^\dagger} V_+^\dagger \\ + V_+^\dagger \frac{\tilde{g}(k,E-\hbar\Omega)}{1-\tilde{g}(k,E-\hbar\Omega)V_+^\dagger\tilde{g}(k,E-2\hbar\Omega)V_+} V_+\Bigg]\Bigg)^{-1} \tilde{g}(k,E) \end{aligned} \tag{4.28}$$

and via the spectral function the band structure can be calculated. Integration over the momentum k then gives the density of states $DOS(E)$, which can not be achieved as easily with the direct approach via the diagonalized Floquet Hamiltonian. This approach is equivalent to the matrix continuous fraction method used to solve other harmonically driven systems [31, 44]. For solving our system like this, a limitation is that we need to add a small imaginary part to the energy in the free Green's function for convergence. This imaginary part leads to a broadening of the quasi-band structure branches. That means, to get the correct result in the numerical integration the k-resolution, at least around the peaks, has to be high enough, which poses an additional numerical challenge. In principle the broadening affects branches of the same sub band equally, but different sub bands will be affected differently. This symmetrical broadening is comparable to the broadening caused by the self-energy in the (self-consistent) Born approximation for the static case for purely electric impurities [34]. The asymmetric behavior due to the interaction of the magnetic and potential part can possibly be modeled by adding small off-diagonal imaginary parts. Another drawback is that the explicit solution for higher cut-offs involves many matrix inversions and will thus get numerically expensive. Since we will only use this method to get rough estimates for the cut-off, we limit ourselves to $n_{max} = 2$ as calculated above. For driving frequencies corresponding to energies bigger than the barrier height this should lead to reasonable results.

In the following subsections we will compare the two band structure approaches for different driving frequencies, put them into context with the response time approach and motivate suitable cut-offs for the impurity system.

4.3.1 High frequency limit

In the high frequency case the separation of the quasi-energy bands is large compared to Δ. The gap size coming from the coupling between the sub bands will be governed by Δ, which in turn means we need to investigate an energy range around $\hbar\Omega/2$ and expect resonances with a width of around Δ. To see these resonances we need an energy resolution lower than Δ. Figure 4.2 shows the results of the two quasi band structure approaches. For the matrix equation case an imaginary part of 10^{-2} was added in the free Green's function. From the response time considerations we expect to need only very few Fourier components and as expected the weight of the first sub band is very low compared to the main band. It can be seen in the inset that focuses on the area of the first crossing. Nonetheless, the avoided crossings lead to resonances in the density of states at $E = \pm\hbar\Omega/2$, as expected, while crossings with the next sub band are not visible at all. Overall, the matrix Green's function band structure coincides with the direct quasi band structure as expected and keeping additional Fourier components (gray dashed lines) does not influence the lower bands. A very low number of Fourier components will give reasonable results.

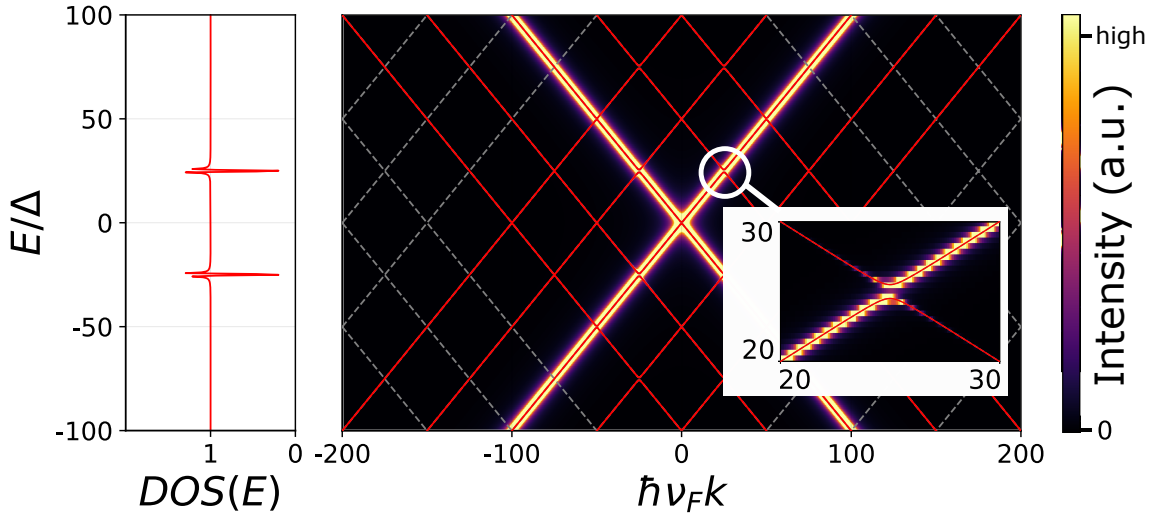

FIG. 4.2: Band structure calculated directly from the Floquet-Hamiltonian (right; red and Grey dashed lines) and directly by keeping the first two Fourier components (right; heatmap) for a homogeneous dynamic magnetic barrier and density of states via integration of the heatmap (left). Floquet parameters: $\hbar\Omega/\Delta = 50.0$, $n_{max} = 2$ (red) and $n_{max} = 10$ (gray).

4.3.2 Around resonance

If we consider driving frequencies closer to $\Delta/\hbar$, which we call resonance from here on, the picture changes. Figure 4.3 shows the results for $\hbar\Omega/\Delta = 0.9$ with an imaginary part of 10^{-3} in the free Green's function. As expected, the direct quasi band structure for $n_{max} = 2$ (red lines) matches the results of the matrix Green's function heatmap. It is clearly visible that the highest bands carry very little weight in this case. Nevertheless, the influence of the higher bands cannot be neglected as the quasi energies are clearly not periodic and the shape of the bands significantly changes when truncating at $n_{max} = 10$ (gray dashed lines). This is a good visualization for the fact that it is important to carry the higher bands even though the Fourier components will be very small. In this case it

means that we need to carry more than two Fourier components to get reasonable results.

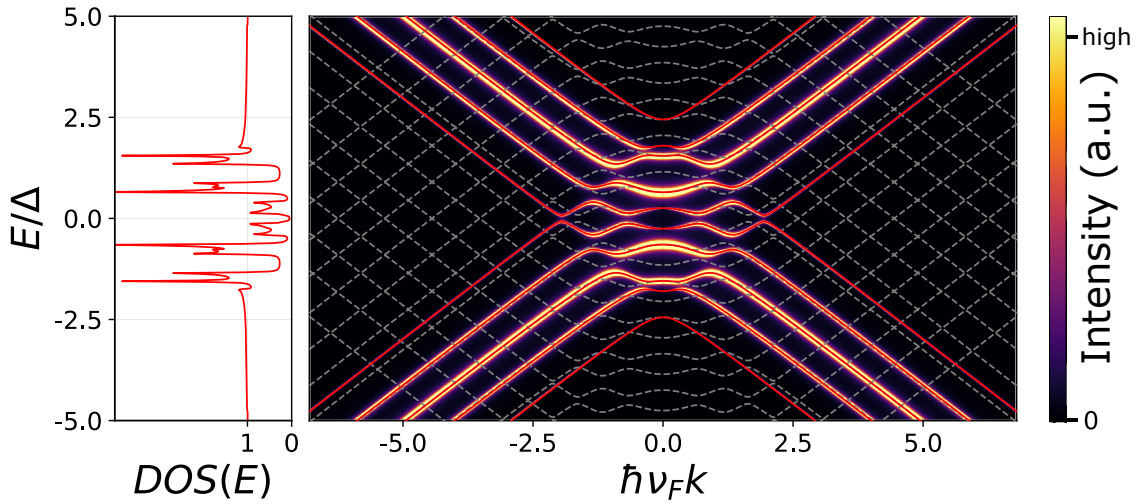

FIG. 4.3: Band structure calculated directly from the Floquet-Hamiltonian (right; red and gray dashed lines) and directly by keeping the first two Fourier components (right; heatmap) for a homogeneous dynamic magnetic barrier and density of states via integration of the heatmap (left). Floquet parameters: $\hbar\Omega/\Delta = 0.9$, $n_{max} = 2$ (red) and $n_{max} = 10$ (gray).

The results for $\hbar\Omega/\Delta = 2.0$ plotted in Fig. 4.4 interestingly show a slightly different picture. Again for $n_{max} = 2$ the spectrum of the Floquet Hamiltonian (red lines) matches the heatmap (calculated with an imaginary part of 10^{-3} in the free Green's function), but here the results for $n_{max} = 10$ (gray dashed lines) do not significantly differ in shape for the populated bands. We can observe a small shift in the band edges, so the edges in the density of states will be slightly shifted towards the gap center.

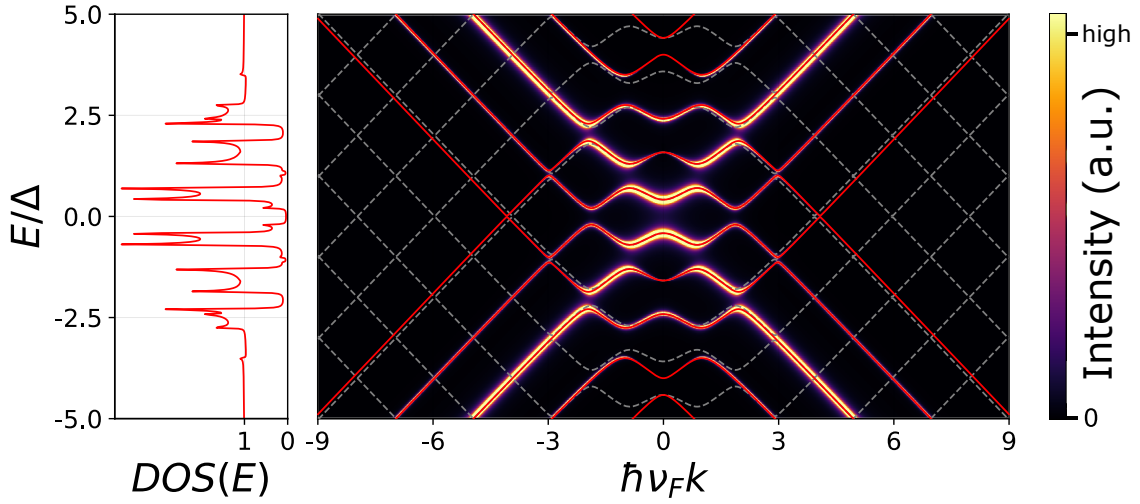

FIG. 4.4: Band structure calculated directly from the Floquet-Hamiltonian (right; red and gray dashed lines) and directly by keeping the first two Fourier components (right; heatmap) for a homogeneous dynamic magnetic barrier and density of states via integration of the heatmap (left). Floquet parameters: $\hbar\Omega/\Delta = 2.0$, $n_{max} = 2$ (red) and $n_{max} = 10$ (gray).

4.3.3 Low frequency limit

For frequencies well below the resonance the response time of the system already suggests that truncation at $n_{max} = 2$ will not give reasonable results and thus the heatmap plot has been disregarded here. In Fig. 4.5 the results of the direct band structure calculations for $\hbar\Omega/\Delta = 0.2$ can be seen for different cut-offs. While the response time considerations suggest that not more than ten bands will be populated, we can clearly see that for $n_{max} = 10$ (blue, right) the periodicity condition is violated. For $n_{max} = 25$ (red, left) the bands are periodic and the results will be reasonable.

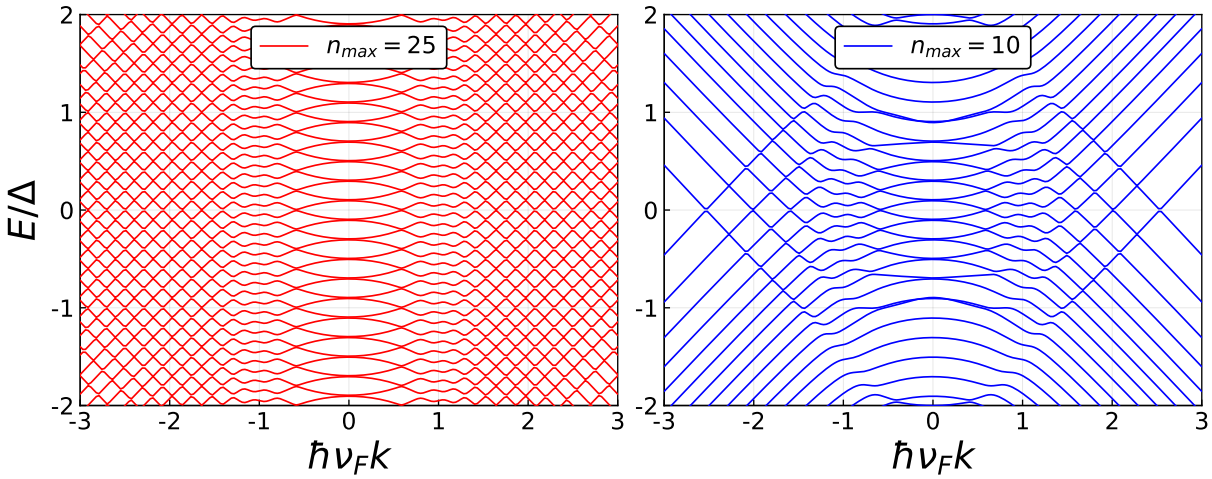

FIG. 4.5: Band structure calculated directly from the Floquet-Hamiltonian for a homogeneous dynamic magnetic barrier. Floquet parameters: $\hbar\Omega/\Delta = 0.2$, $n_{max} = 25$ (red) and $n_{max} = 10$ (blue).

4.4 Impurity averaging

Solving the matrix Eq. (3.21) allows us to calculate the Green's function and therefore the density of states for one specific impurity distribution. That could be measured by probing the density of states or spectral function locally, for example at an impurity site. In reality we are usually not interested in these local properties, but in averages over larger areas that govern for example the transport properties. They can be accessed by averaging over many local measurements or probing larger areas. Therefore, we will employ a numerical impurity averaging procedure by creating random impurity distributions and averaging over the density of states in the center of the impurity region for a large number of random distributions. We use the results for the center impurity to avoid tunneling contributions due to the finite system length. This averaging method corresponds to lining up many random impurity areas up to a long, realistic system. Note here, that $M(t)$, and therefore $V_{\pm}$, does not change for different impurity distributions (we assume a uniform rotation of all the magnetic moments) with the same number of impurities. Only $\tilde{g}(E)$ has to be adapted for each impurity distribution.

The program has been run in 10 batches of 100 random impurity distributions, meaning the Green's function was calculated for 100 random impurity distributions, averaged over these, saved to a file and then repeated 10 times. This was done mainly do avoid filling the hard drive with unnecessary data, since we are not interested in the results

for single distributions. Running it in these smaller batches still gives a way of checking the convergence, without saving an excessive number of files. The batch size can be adapted in the program if the convergence is ensured otherwise. To get the end result of $n_{runs} = 1000$ impurity averaging runs the average over these 10 batches is calculated. If we denote the results of single batches by $DOS_i(E)$ we can write the standard deviation from the end result $DOS(E)$ for $N = 10$ batches as

$$Std(E) = \sqrt{\frac{\sum_{i=1}^{N} \left(DOS_i(E) - DOS(E)\right)^2}{N-1}}. \tag{4.29}$$

To see the effect of averaging over more impurity distributions we can replace $DOS_i(E)$ with means of several batches, i.e. using for example all possible combinations of two distinct batches (corresponds to averaging over 200 impurity distributions), and take the standard deviation over all these combinations. In the case of $N = 2$ this means we take every possible distinct combination of two batches and calculate the average for all the combinations. That leaves us with $10!/(10-2)!$ possible results for averaging over 200 impurity distributions that we can calculate from our 10 batches. For these then the standard deviation from the average over all runs is calculated. Figure 4.6 shows the resulting averaged density of states (bottom) along with the standard deviation from the results for every possible combination of batch-averages for the given number of runs for typical parameters. It can be seen that the biggest standard deviation for averages over 900 runs is around 0.01 , which means, that if we take the average over any 9 of the batches instead of all 10 batches, the result will on average not differ more than that. This shows that the impurity averaging already converges well enough to not obstruct the prominent features. This is also the case for other relevant parameters, for some of which similar plots can be found in Appendix C.

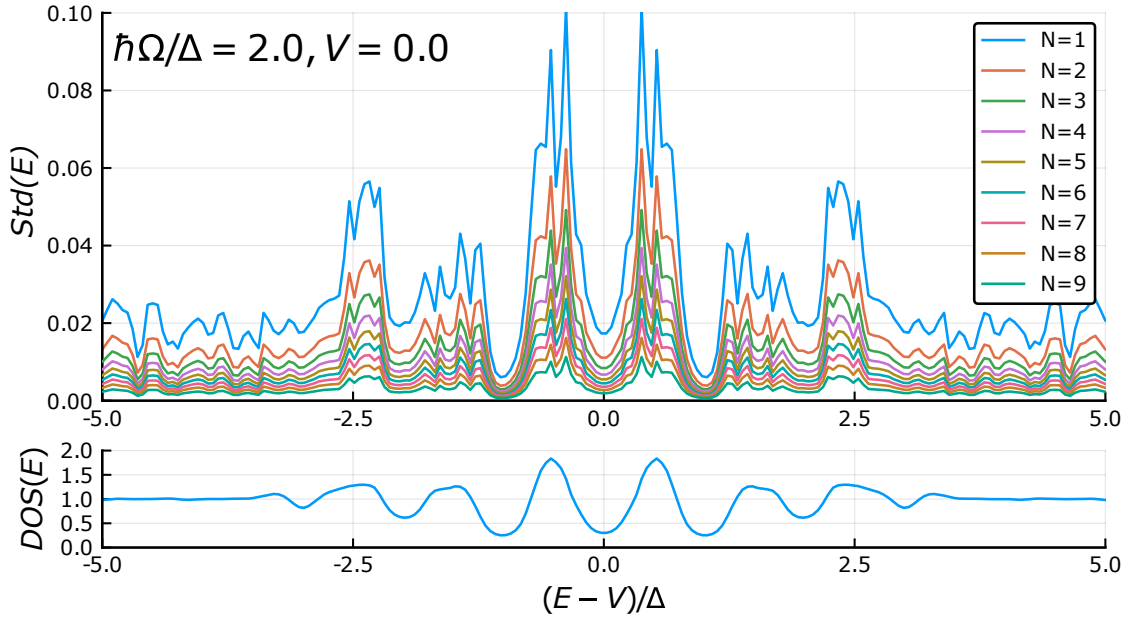

FIG. 4.6: Standard deviation from the mean over 10 batches (100 runs per batch) for all possible combinations of N batches. Floquet parameters: $\hbar\Omega/\Delta = 2.0$, $n_{max} = 6$. Impurity parameters: $M/\hbar\nu_F = 0.2$, $V/M = 0$, $L/l_\Delta = 8.0$

5 Results and discussion

In this chapter we will solve the matrix Eq. (3.21) for reasonable parameters and compare the resulting density of states for equally spaced impurities that can be seen as a discrete limit of a homogeneous barrier with results for randomly distributed impurities with impurity averaging. Additionally, we will compare to appropriate results obtained by other means. The discussion will be divided into two parts. Firstly, a part dealing with purely magnetic impurities that can be directly compared to different approaches for a homogeneous barrier and, secondly, a section where we investigate the influence of the potential part more closely. Note here, that the results are the impurity averaged density of states at the center of the impurity region, i.e. to calculate the density of states the sub-matrix of $G(E)$ corresponding to the impurity closest to the center is picked. This is done to minimize tunneling contributions and to be able to compare to realistic, much bigger systems, as already discussed in section 4.4.

5.1 Purely magnetic impurities

As before, the discussion focuses on the high–, resonant– and low–frequency case separately.

5.1.1 High frequency limit

For high driving frequencies we expect a flat density of states for an energy range of a few Δ around 0 and additional resonances at $E = \pm\hbar\Omega/2$. Thus, the energy range has been chosen large compared to the static impurity gap size. In Fig. 5.1 the density of states for equally (blue) and randomly distributed (red) impurities for $\hbar\Omega = 50.0$ along with the density of states from the homogeneous barrier (gray dashed) from Fig. 4.2 (left) is shown. As expected, the resonances at $E = \pm\hbar\Omega/2$ can be seen in all three curves and while the random impurity curve matches the homogeneous barrier very well, there are additional resonances in the equally distributed impurity case. The regular structure and the fact that the resonances are not present in the impurity averaged case hint at a connection to the equal spacing of the impurities. For random impurity distributions the resonances at $E = \pm\hbar\Omega/2$ can also be seen, but there are no distinct additional resonances as the curves look mainly like noise (not shown). The spacing changes for different impurity strength M (not shown). Since the numerical model determines the number of impurities in the interval, and thereby the impurity distance, via the impurity strength, it is not obvious whether the effect depends on the impurity strength, the position/distance or both. This could in principle be investigated closer with slight alterations in the program and parameters. Furthermore, for different, high driving frequencies (not shown) the features also move in such a way that resonances lie at $E = \pm\hbar\Omega/2$ and a coincidental match can be excluded. The higher order resonances at $E = \pm 3\hbar\Omega/2$ are not visible in any of the curves. Since in the static case the impurities lead to a broadening of the branches in the band structure, the higher order resonances could be very narrow and are thus likely washed out and thereby suppressed.

5.1.2 Around resonance

Figure 5.2 shows the density of states for two different frequencies around the resonance. As expected from the considerations in section 4.3, the results from the homogeneous

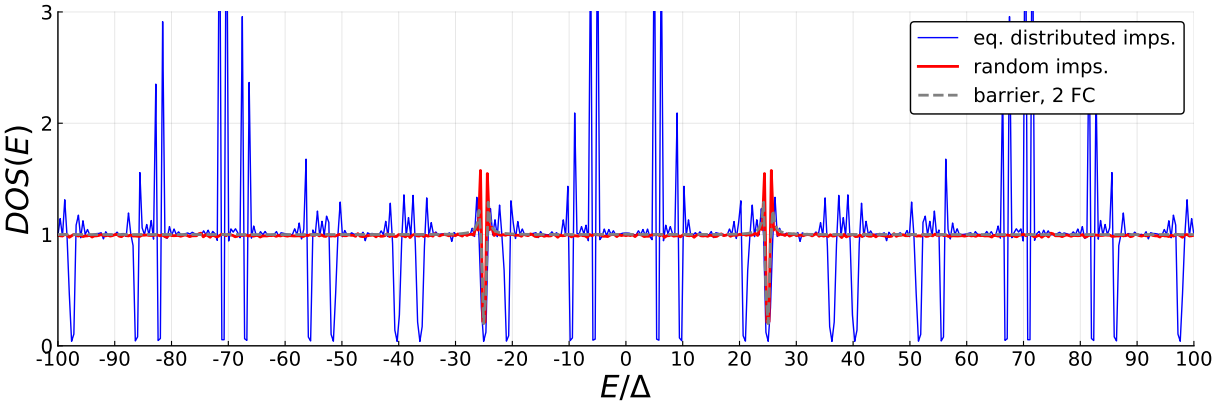

FIG. 5.1: High driving frequency density of states as a function of energy for equally distributed impurities (blue), random impurities averaged over $N_{runs} = 1000$ distributions (red) and for a homogeneous barrier keeping two Fourier components (gray). Floquet parameters: $\hbar\Omega/\Delta = 50.0$, $n_{max} = 3$. Impurity parameters: $M/\hbar\nu_F = 0.2$, $L/l_\Delta = 8.0$

barrier (gray dashed) do not match very well for $\hbar\Omega/\Delta = 0.9$ (upper). Interestingly, the biggest resonance peaks still match the position of the main peaks for the equally distributed (blue) and random (red) impurities but coincidence cannot be excluded from this. For $\hbar\Omega/\Delta = 2.0$ (lower) the gap positions for equally distributed (blue) and random (red) impurities follow the predictions from the homogeneous barrier with a slight shift towards $E = 0$. This is consistent with the observation that higher bands in this case only push the lower bands towards the center, while they do not change the shape of the bands significantly. The impurity nature of the system in both cases washes the structures out and as expected that effect is stronger for the impurity averaging case when compared to the equally distributed impurities.

In both cases we can also observe that the density of states is flat for bigger energies and that the deeper dips lie closer to the center. This suggests that the higher quasi energy bands cannot be populated. Since higher bands correspond to higher Fourier components and therefore a faster dynamic, these findings are consistent with the response time considerations from section 4.3. Additionally, for energies beyond the static band gap edge $\pm\Delta$ tunneling trough the barrier should become significant and may contribute to this effect.

5.1.3 Low frequency limit

As before, the density of states for the homogeneous barrier truncating at $n_{max} = 2$ will not be usable in the low frequency case. Since in the low frequency limit the response time of the system is much faster than the rotation of the impurities, we can assume the density of states at a time t to correspond to the static density of states for the impurity orientation at that time. The density of states from the matrix Green's function being the average over one driving period allows us to compare the numerical results to the average over the density of states for several static impurity orientations. The results for the static cases have been calculated via the self-consistent Born approximation described in Ref. [34]. Figure 5.3 shows the results from the numerical approach again for equally spaced impurities (blue), impurity averaging (red) and averaging over static impurity densities of states (gray dashed), matching reasonably well.

We can better understand the shape of the density of states in the picture of the quasi

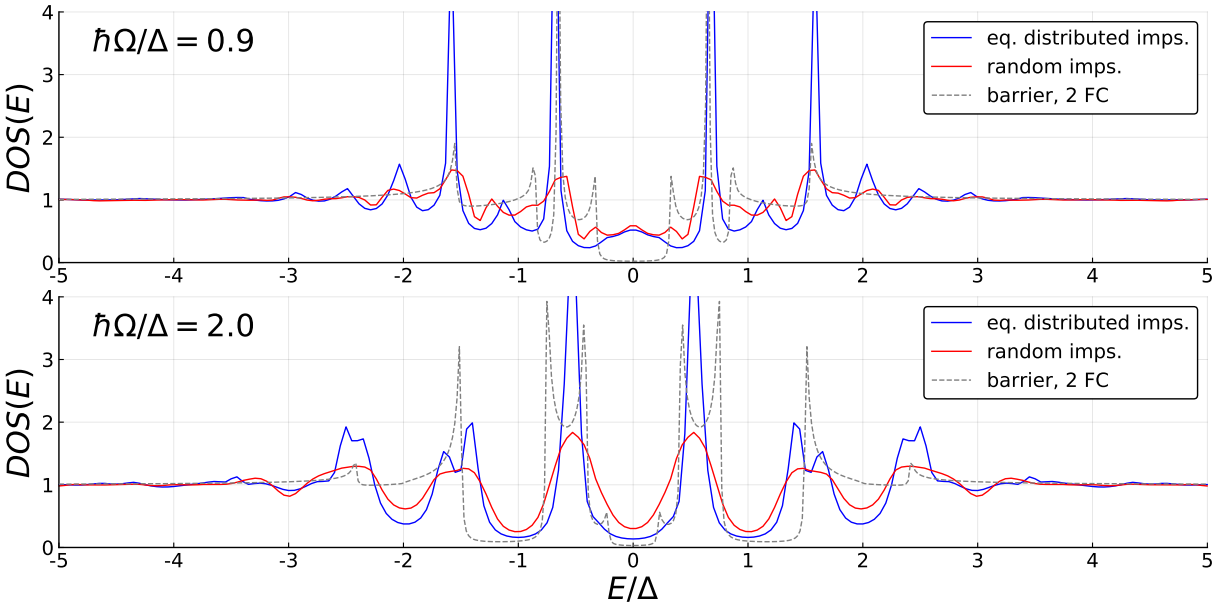

FIG. 5.2: Density of states as a function of energy for equally distributed impurities (blue), random impurities averaged over $N_{runs} = 1000$ distributions (red) and for a homogeneous barrier keeping two Fourier components (gray) for driving with $\hbar\Omega \approxeq \Delta$. Floquet parameters: $\hbar\Omega/\Delta = 0.9$, $n_{max} = 10$ (top) and $\hbar\Omega/\Delta = 2.0$, $n_{max} = 6$ (bottom). Impurity parameters: $M/\hbar\nu_F = 0.2$, $L/l_\Delta = 8.0$

energy sub bands. From previous considerations we know that we need a big number of sub bands. The sub bands corresponding to a frequency close to the resonance of the system will be the preferred sub band while the lower bands are progressively less populated and thereby lead to the descending shape of inside the static gap. The biggest difference between the self-consistent Born approximation average and the matrix Green's function results is the behavior around $E = 0$, where the former declines almost to zero, while the latter match very well and take on a finite value. This can be explained taking into consideration, that the self-consistent Born approximation treats an infinite impurity region, while in the numerics the impurity region is finite and thus for small gaps tunneling through the impurity region contributes to the density of states.

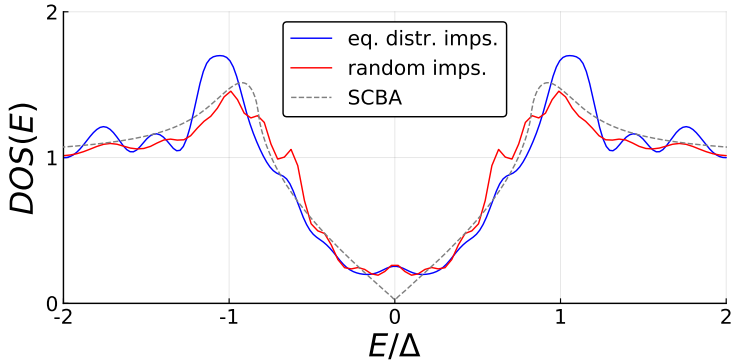

FIG. 5.3: Low driving frequency density of states as a function of energy for equally distributed impurities (blue), random impurities averaged over $N_{runs} = 1000$ distributions (red) and via averaging over static self-consistent Born approximation results (gray). Floquet parameters: $\hbar\Omega/\Delta$, $n_{max} = 25$. Impurity parameters: $M/\hbar\nu_F = 0.2$, $L/l_\Delta = 8.0$, SCBA: average over results for 1000 static impurity orientations equally distributed in the $x - y$-plane.

5.2 Influence of the potential part

The previous section introduced the impurity nature of the system for purely magnetic impurities. It already became apparent that the impurities lead to a broadening of the resonances. From the homogeneous barrier the positions of the resonances can still be predicted, but there the potential part will only lead to a shift of the density of states by V, while it stays symmetric around the gap center. For static impurities the impurity potential part introduces an asymmetry and ultimately flattens the density of states [34]. This can be explained by comparing to the homogeneous case and looking at the heatmap plots in section 4.3. In the heatmaps, e.g. Fig. 4.2, it is clearly visible that some bands carry more weight than others. The potential part now causes an energy shift that moves the features away from the area, where the bands carry weight. Especially, if the potential part moves the features up in energy, the features below the center gain weight and will enhanced until they pass the center, while the features above are weakened. We expect a similar behavior in the dynamic case. As before three separate driving frequency ranges are investigated.

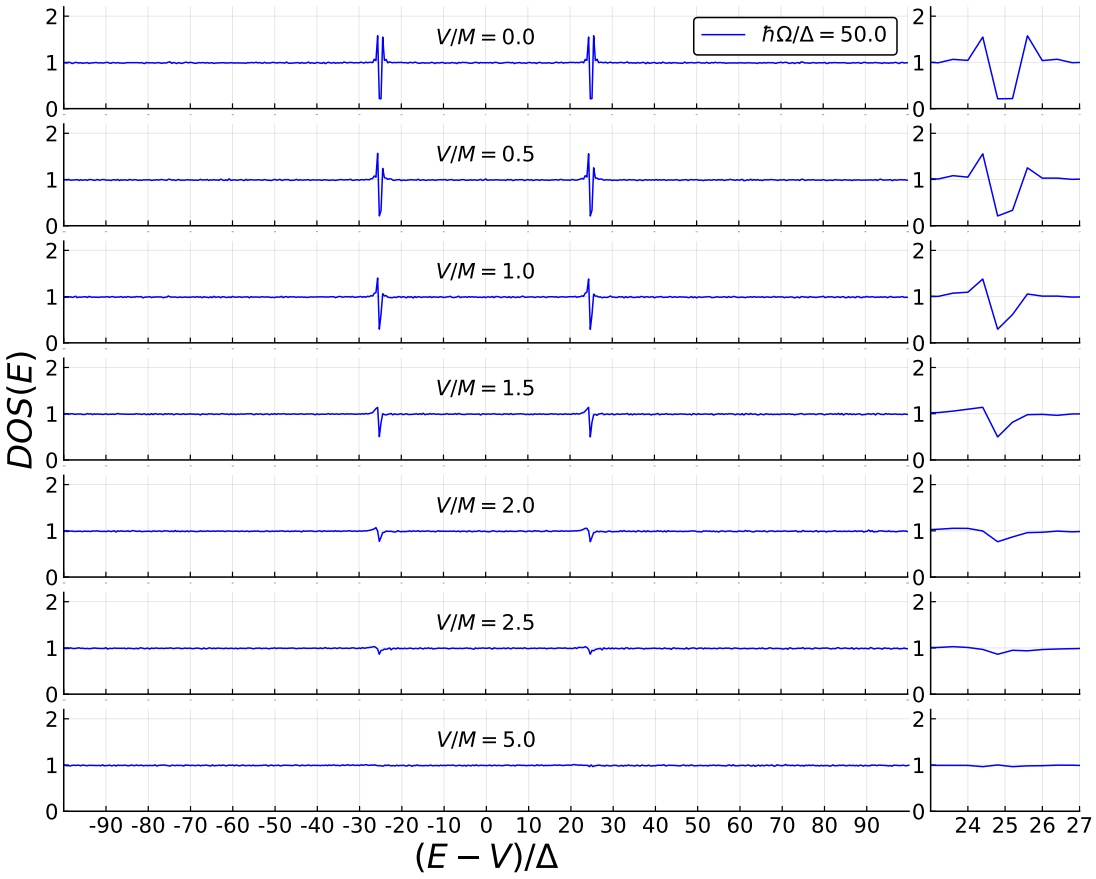

FIG. 5.4: High driving frequency density of states as a function of energy for different potential strengths with details around one resonance. Floquet parameters: $\hbar\Omega/\Delta = 50.0$ and $n_{max} = 3$. Impurity parameters: $N_{runs} = 1000$, $M/\hbar\nu_F = 0.2$, $L/l_\Delta = 8.0$

5.2.1 High frequency limit

For the high frequency case we again chose the number of Fourier components according to the estimations earlier. In Fig. 5.4 the density of states for different potential strengths

is shown. Again we can see resonances at $\pm\hbar\Omega/2\Delta$, while the higher resonances at $\pm 3\hbar\Omega/2\Delta$ do not appear. For small potential parts they are simply shifted by V and show a slight asymmetry, while for strong potentials they disappear completely and we find a flat density of states. This is an inherent property of the magnetic impurity system, since for a barrier the potential contribution merrily shifts the level energy levels equally. In the static impurity case the potential contribution leads to a non-zero imaginary self-energy in the Dyson-equation [34] and thus broadens the energy branches. Similarly, this effect washes the dynamic resonances out.

5.2.2 Around resonance

For the two cases around resonance, displayed in Fig. 5.5, the asymmetry introduced by the potential part is well visible. Small values sharpen some of resonance visibly, while for rising potential part the density of states quickly flattens. For $\hbar\Omega/\Delta = 2.0$ (blue) the first resonance below zero is already shrinking at $V = 1.0$ while for $\hbar\Omega/\Delta = 0.9$ (red) this does not seem to be the case. The driving frequency might have an effect on how strong the influence of the potential part is. Looking at development until $V = 5.0$ one can suspect that the lower driving frequency reduces the flattening due to V, but it is not entirely clear from this data.

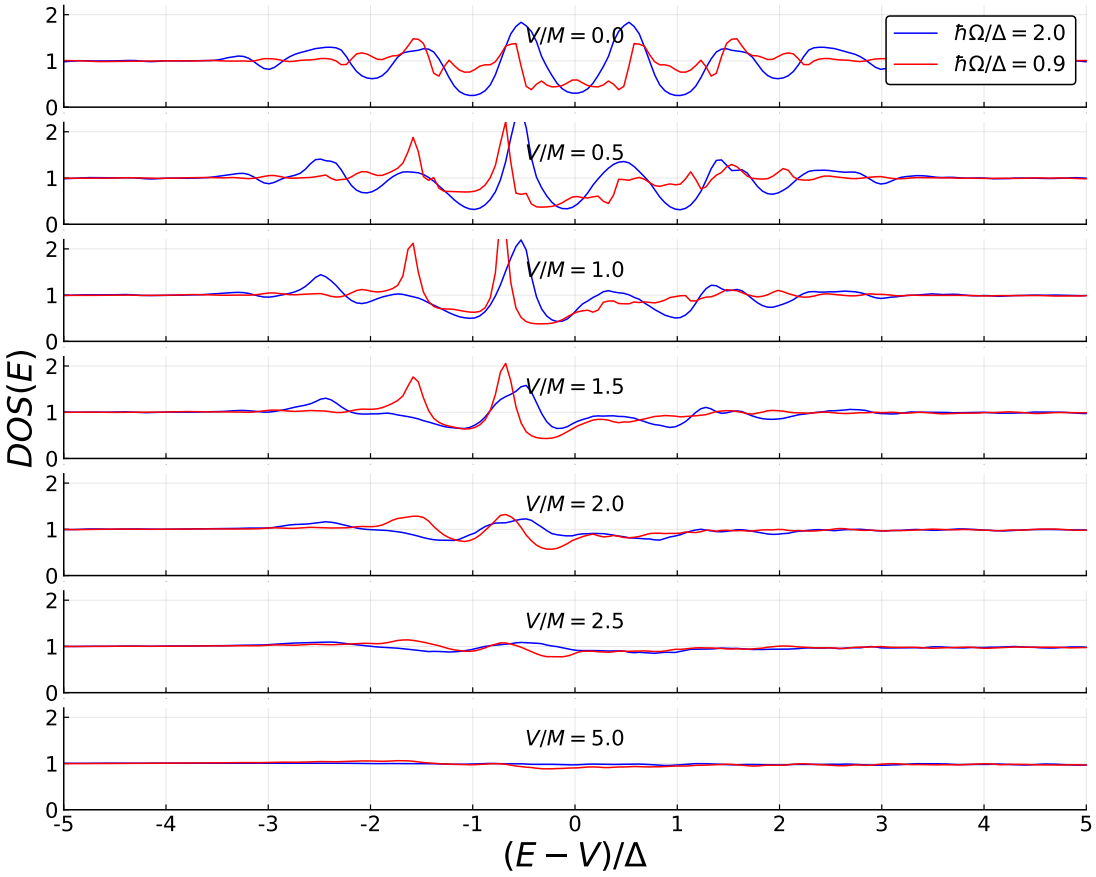

FIG. 5.5: Density of states as a function of energy for different potential strengths for driving with $\hbar\Omega \approxeq \Delta$. Floquet parameters: $\hbar\Omega/\Delta = 2.0$, $n_{max} = 6$ (blue) and $\hbar\Omega/\Delta = 0.9$, $n_{max} = 10$ (red). Impurity parameters: $N_{runs} = 1000$, $M/\hbar\nu_F = 0.2$, $L/l_\Delta = 8.0$

5.2.3 Low frequency limit

In the low frequency limit we can again compare the numeric results to the self-consistent Born approximation averaged over many impurity orientations , since the response time of the system is much faster than the driving. Figure 5.6 shows the matrix equation results (blue) along with the self-consistent Born approximation results (gray). The curves match reasonably well, only showing a slight shift, confirming that the average over static results is suitable for the slow driving case. As the matrix equation in the static case reduces to an equation matching the self-consistent Born approximation very well [34] this is not surprising and confirms that there are no additional effects when driving significantly slower than the system response time.

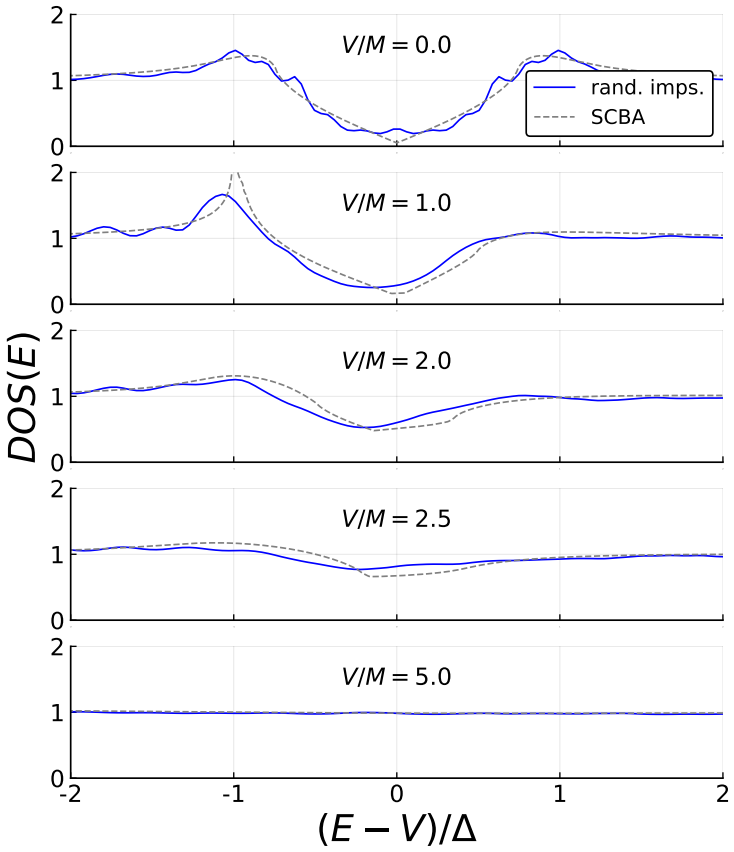

FIG. 5.6: Density of states as a function of energy for different potential strengths from the matrix equation (blue) and via averaging over static self-consistent Born approximation results (gray). Floquet parameters: $\hbar\Omega/\Delta = 0.2$ and $n_{max} = 25$. Impurity parameters: $N_{runs} = 1000$, $M/\hbar v_F = 0.2$, $L/l_\Delta = 8.0$, SCBA: average over results for 1000 impurity orientations equally distributed in the $x-y$-plane.

6 Summary and outlook

Here we will give a short summary of the results of this thesis, also considering the methods and limitations. Moreover, we will give an overview over which aspects might deserve further investigation and in what direction the project will be developed for the preparation of a manuscript.

In section 1, after a brief overview over the field and the history of TIs, we gave a visualization of the model we are working with in this thesis. Section 2 addressed the basic toolkit and introduced the model Hamiltonian on which this thesis is build. The concept of the single particle Green's function has been established to access the density of states of a system via the spectral function. The necessary basics of Floquet theory have been explained and applied to a two-level system. Subsequently, the BHZ model has been introduced. To construct the random edge impurity Hamiltonian Eq. (2.39), the effective 2×2 edge Hamiltonian has been presented and after demonstrating the effects of a magnetic field in this system, the impurity potential has been introduced. The main limitation of this effective edge Hamiltonian is that it neglects the presence of bulk states and is only valid for energies well within the bulk band gap, defined by the BHZ parameters. In our case, this limitation is not very severe due to the scaling in terms of the static impurity gap $\Delta = nM$ we applied. By tuning the impurity density, in principle, we can always choose to operate on a small enough energy scale. To compare with a real experiment, one would then have to check, if the parameters are in a range, where our model is applicable. To investigate the effect taking in consideration the in the bulk states the full 4×4 BHZ Hamiltonian would have to be considered.

Since one of the most important parts of the problem is finding the Green's function, section 3 was dedicated to deriving a very general matrix equation for a broad range of time-periodic Hamiltonians. The derived matrix Eq. (3.16) can also be solved for more complicated periodic Hamiltonians, although the numerical costs can be very high, since then the block-tridiagonal structure is lost. For harmonically driven systems Eq. (3.21) follows directly and this is the main result that was used in the following chapters.

Section 4 was dedicated to applying the matrix Eq. (3.21) to our model Hamiltonian. A big part of this was finding suitable finite cut-offs for the model, so the matrix equations can be numerically solved. On the one hand the impurity system leads to a $2N_{imp} \times 2N_{imp}$ matrix (factor two due to the spin), so the number of impurities has to be limited. That has to be done considering tunneling through the impurity region as well. On the other hand it is important to get a reasonable cut-off for the Fourier series expansion of the Green's function. It turned out that to get a valid results, not only the response time of the system has to be considered, but also the shape of the Floquet sub bands. The quasi-band structure has been found for a homogeneous magnetization that can be treated in momentum space via the matrix Eq. (3.21). This combination leads to the result that for small driving frequencies the number of Fourier components that need to be carried is a lot higher than for high frequency driving. That means that slow driving is numerically more expensive in this model. Finally, to treat the random impurities, we introduced an impurity averaging procedure.

The results were presented in section 5 in the form of density of states plots. As in section 4, the discussion was divided in low, resonance and high frequency driving. First the three cases were treated for purely magnetic impurities. The considerations in section 4 have been used as a comparison here, along with results for equally spaced impurities. The equally spaced impurities can be seen as a discrete limit of a homogeneous magnetic

barrier and are therefore suitable as a comparison. The density of states plots show the influence of the random impurities on the system. In the resonance case instead of sharp resonances the peaks for random impurities are strongly broadened, while for fast driving the low energy density of states is flat. For higher energies peaks related to the Floquet sub band crossings appear. Equally spaced impurities lead to additional, somewhat regular resonances. For slow driving the results match well with the average over the density of states for static systems with different impurity orientations. These averages have been calculated using methods from an earlier work [34], namely the self-consistent Born approximation. Similar to our previous works, here the influence of the potential part was considered. As expected from the results for static impurities, the features in the density of states get flattened for increasing potential part in all considered cases. For a high enough potential part the density of states is flat again, as is the case for a clean system.

Within this project there are some parts that have not been investigated in detail. For example, the additional resonances appearing for equally spaced impurities have not been fully explained. The most obvious explanation would be a Fabry-Pérot like resonance behavior due to the equal spacing, but to get certainty about that a closer investigation is needed.

Secondly, this model is focusing on the rotation of impurities in the x-z-plane. Due to the general form of Eq. (3.21) it is easily possible to adapt the model for a rotation, for example in the x-y-plane. That particular case would be interesting, since the density of states in the static case does not depend on the orientation of the magnetic moment in the x-y-plane. For slow driving one would expect a gapped density of states exactly like the static case, while for fast driving the magnetic moments should average out and give a flat density of states again. The transition between these two limit cases could potentially be interesting.

The general nature of Eq. (3.21) also allows to treat cases like purely electric periodic impurities. It might be interesting to compare the results this model produces with results for a single dynamic electric impurity like in Ref. [31], especially since solving the matrix equation should be equivalent to the matrix continued fraction method used there.

In previous works we also used the self-consistent Born approximation for static impurities. Similar to what has been done on Ref. [34], we should be able to apply the self-consistent Born approximation to the Floquet-Hamiltonian of the impurity system. Note here, that this is not the comparison that has been made for the low frequency case, since there we averaged over results for static impurities. Applying the self-consistent Born approximation to the Floquet-Hamiltonian would allow us to also investigate driving regimes other than low frequencies. This would be a good comparison to the numeric model and could be used to see the influence of scattering processes corresponding to crossing diagrams, which are neglected in the self-consistent Born approximation.

The focus of the manuscript we want to write following this thesis is now accessing the transport properties, e.g. the conductance, since they are related to the Greens function. An interesting aspect here will be, that due to spin-momentum locking in the edge channels with the charge there is also spin transport happening. This analysis will require the matrix equation for the edge impurity Hamiltonian to be written in a slightly different form. The main procedure will still be the same and this thesis will serve as a basis for the planned publication.

In the more distant future it could be interesting to look at the effects of interaction. Due to the nature of the single particle Green's function used here interaction effects are

not included. In 3D TIs these have been shown to have an influence and cause additional gap opening mechanisms [35].

As one of the now most active fields in condensed matter physics the theory on topological materials is developing rapidly. At the same time more and more experiments are realized and a better understanding of the fundamental effects is being reached. On of the most intriguing fields for the application of TIs certainly is topological quantum computation. Using the intrinsic properties like dissipationless transport in the edge channels also opens up applications in low-power information processing or spintronics. This suggests, that TIs are going to stay a promising and important research area in the future.

References

[1] T. Ando, Y. Matsumoto, and Y. Uemura, J. Phys. Soc. Jpn. **39**, 279 (1975).

[2] J.-i. Wakabayashi and S. Kawaji, J. Phys. Soc. Jpn. **44**, 1839 (1978).

[3] R. E. Prange and S. M. Girvin, eds., *The quantum hall effect* (Springer New York, 1990).

[4] H. Ibach and H. Lüth, *Solid-state physics* (Springer, 2010).

[5] K. v. Klitzing, G. Dorda, and M. Pepper, Phys. Rev. Lett. **45**, 494 (1980).

[6] X.-L. Qi and S.-C. Zhang, Rev. Mod. Phys. **83**, 1057 (2011).

[7] B. A. Bernevig, T. L. Hughes, and S.-C. Zhang, Science **314**, 1757 (2006).

[8] M. König, S. Wiedmann, C. Brüne, A. Roth, H. Buhmann, L. W. Molenkamp, X.-L. Qi, and S.-C. Zhang, Science **318**, 766 (2007).

[9] M. Z. Hasan and C. L. Kane, Rev. Mod. Phys. **82**, 3045 (2010).

[10] G. M. Gusev, Z. D. Kvon, E. B. Olshanetsky, A. D. Levin, Y. Krupko, J. C. Portal, N. N. Mikhailov, and S. A. Dvoretsky, Phys. Rev. B **89**, 125305 (2014).

[11] G. Grabecki, J. Wróbel, M. Czapkiewicz, . Cywiski, S. Gieratowska, E. Guziewicz, M. Zholudev, V. Gavrilenko, N. N. Mikhailov, S. A. Dvoretski, F. Teppe, W. Knap, and T. Dietl, Phys. Rev. B **88**, 165309 (2013).

[12] K. C. Nowack, E. M. Spanton, M. Baenninger, M. König, J. R. Kirtley, B. Kalisky, C. Ames, P. Leubner, C. Brüne, H. Buhmann, L. W. Molenkamp, D. Goldhaber-Gordon, and K. A. Moler, Nat. Mater. **12**, 787 (2013).

[13] A. Roth, C. Brüne, H. Buhmann, L. W. Molenkamp, J. Maciejko, X.-L. Qi, and S.-C. Zhang, Science **325**, 294 (2009).

[14] C. Liu, T. L. Hughes, X.-L. Qi, K. Wang, and S.-C. Zhang, Phys. Rev. Lett. **100**, 236601 (2008).

[15] I. Knez, R.-R. Du, and G. Sullivan, Phys. Rev. Lett. **107**, 136603 (2011).

[16] K. Suzuki, Y. Harada, K. Onomitsu, and K. Muraki, Phys. Rev. B **87**, 235311 (2013).

[17] I. Knez, C. T. Rettner, S.-H. Yang, S. S. Parkin, L. Du, R.-R. Du, and G. Sullivan, Phys. Rev. Lett. **112**, 026602 (2014).

[18] E. M. Spanton, K. C. Nowack, L. Du, G. Sullivan, R.-R. Du, and K. A. Moler, Phys. Rev. Lett. **113**, 026804 (2014).

[19] H. Zhang, C.-X. Liu, X.-L. Qi, X. Dai, Z. Fang, and S.-C. Zhang, Nat. Phys. **5**, 438 (2009).

[20] H.-J. Zhang, C.-X. Liu, X.-L. Qi, X.-Y. Deng, X. Dai, S.-C. Zhang, and Z. Fang, Phys. Rev. B **80**, 085307 (2009).

[21] C.-Z. Chang, J. Zhang, X. Feng, J. Shen, Z. Zhang, M. Guo, K. Li, Y. Ou, P. Wei, L.-L. Wang, Z.-Q. Ji, Y. Feng, S. Ji, X. Chen, J. Jia, X. Dai, Z. Fang, S.-C. Zhang, K. He, Y. Wang, L. Lu, X.-C. Ma, and Q.-K. Xue, Science **340**, 167 (2013).

[22] X. Liu, H.-C. Hsu, and C.-X. Liu, Phys. Rev. Lett. **111**, 086802 (2013).

[23] Y. Ren, J. Zeng, X. Deng, F. Yang, H. Pan, and Z. Qiao, Phys. Rev. B **94**, 085411 (2016).

[24] R. Yu, W. Zhang, H.-J. Zhang, S.-C. Zhang, X. Dai, and Z. Fang, Science **329**, 61 (2010).

[25] N. Nagaosa, J. Sinova, S. Onoda, A. H. MacDonald, and N. P. Ong, Rev. Mod. Phys. **82**, 1539 (2010).

[26] C.-X. Liu, S.-C. Zhang, and X.-L. Qi, Annu. Rev. Condens. Matter Phys. **7**, 301 (2016).

[27] S. Cho, N. P. Butch, J. Paglione, and M. S. Fuhrer, Nano Lett. **11**, 1925 (2011).

[28] L. Fu and C. L. Kane, Phys. Rev. Lett. **100**, 096407 (2008).

[29] Z. Yue, B. Cai, L. Wang, X. Wang, and M. Gu, Sci. Adv. **2**, e1501536 (2016).

[30] Z. Yue, G. Xue, J. Liu, Y. Wang, and M. Gu, Nat. Commun. **8**, 15354 (2017).

[31] S. Pradhan and J. Fransson, Phys. Rev. B **100**, 125163 (2019).

[32] Q.-Z. Wang, X. Liu, H.-J. Zhang, N. Samarth, S.-C. Zhang, and C.-X. Liu, Phys. Rev. Lett. **113**, 147201 (2014).

[33] A. M. Black-Schaffer, A. V. Balatsky, and J. Fransson, Phys. Rev. B **91**, 201411 (2015).

[34] S. Wozny, K. Vyborny, W. Belzig, and S. I. Erlingsson, Phys. Rev. B **98**, 165423 (2018).

[35] A. C. Balram, K. Flensberg, J. Paaske, and M. S. Rudner, Phys. Rev. Lett. **123**, 246803 (2019).

[36] B. Zhou, H.-Z. Lu, R.-L. Chu, S.-Q. Shen, and Q. Niu, Phys. Rev. Lett. **101**, 246807 (2008).

[37] X. Liu and J. K. Furdyna, J. Phys.: Condens. Matter **18**, R245 (2006).

[38] S. A. Crooker, J. J. Baumberg, F. Flack, N. Samarth, and D. D. Awschalom, Phys. Rev. Lett. **77**, 2814 (1996).

[39] H. Bruus and K. Flensberg, *Many-body quantum theory in condensed matter physics* (OUP Oxford, Sept. 2, 2004), 464 pp.

[40] S. Doniach and E. H. Sondheimer, *Green's functions for solid state physicists* (Imperial College Press, Jan. 9, 1998), 336 pp.

[41] M. Grifoni and P. Hänggi, Phys. Rep. **304**, 229 (1998).

[42] F. GroSSmann, P. Jung, T. Dittrich, and P. Hänggi, Z. Phys. B **84**, 315 (1991).

[43] J. S. Howland, Math. Ann. **207**, 315 (1974).

[44] D. F. Martinez, J. Phys. A **36**, 9827 (2003).

[45] H. Sambe, Phys. Rev. A **7**, 2203 (1973).

[46] H.-J. Schmidt, Z. Naturforsch. A **73**, 705 (2018).

[47] J. H. Shirley, Phys. Rev. **138**, B979 (1965).

[48] G. Platero and R. Aguado, Phys. Rep. **395**, 1 (2004).

[49] M. S. Rudner and N. H. Lindner, (2019), arXiv:1909.02008v1.

[50] D. Curcio, A. J. H. Jones, R. Muzzio, K. Volckaert, D. Biswas, C. E. Sanders, P. Dudin, C. Cacho, S. Singh, K. Watanabe, T. Taniguchi, J. A. Miwa, J. Katoch, S. Ulstrup, and P. Hofmann, (2020), arXiv:2001.09891v1.

[51] M. König, H. Buhmann, L. W. Molenkamp, T. Hughes, C.-X. Liu, X.-L. Qi, and S.-C. Zhang, J. Phys. Soc. Jpn. **77**, 031007 (2008).

[52] J. Linder, T. Yokoyama, and A. Sudbø, Phys. Rev. B **80**, 205401 (2009).

[53] H.-Z. Lu, W.-Y. Shan, W. Yao, Q. Niu, and S.-Q. Shen, Phys. Rev. B **81**, 115407 (2010).

[54] M. Wada, S. Murakami, F. Freimuth, and G. Bihlmayer, Phys. Rev. B **83**, 121310 (2011).

[55] Q. Chen, L. Du, and G. A. Fiete, Phys. Rev. B **97**, 035422 (2018).

[56] F. Tricomi, *Integral equations*, (Pure and applied mathematics, v. 5) (Dover Publications, 1985).

[57] J. Strunz, J. Wiedenmann, C. Fleckenstein, L. Lunczer, W. Beugeling, V. L. Müller, P. Shekhar, N. T. Ziani, S. Shamim, J. Kleinlein, H. Buhmann, B. Trauzettel, and L. W. Molenkamp, Nat. Phys. **16**, 83 (2020).

Appendices

A Residue theorem calculations

In this appendix residue theorem calculations are performed in order to transform momentum domain Green's functions into position space for various cases.

A.1 Homogenous magnetic field

In this section we perform the residue calculations to calculate the density of states from the momentum domain Green's function

$$G(k,E) = \frac{E + \hbar\nu_F k\sigma_z + \Delta\sigma_x}{E^2 - (\hbar\nu_F k)^2 - \Delta^2}. \tag{A.1}$$

Formally, we can write

$$G(x,x',E) = \int_{-\infty}^{\infty} \frac{\mathrm{d}k}{2\pi} G(k,E) e^{\mathrm{i}k(x-x')} \tag{A.2}$$

$$= \int_{-\infty}^{\infty} \frac{\mathrm{d}k}{2\pi} \frac{E + \hbar\nu_F k\sigma_z + \Delta\sigma_x}{E^2 - (\hbar\nu_F k)^2 - \Delta^2} e^{\mathrm{i}k(x-x')} \tag{A.3}$$

$$= \frac{1}{\hbar\nu_F} \int_{-\infty}^{\infty} \frac{\mathrm{d}k}{2\pi} \frac{E + k\sigma_z + \Delta\sigma_x}{E^2 - k^2 - \Delta^2} e^{\mathrm{i}\frac{k}{\hbar\nu_F}(x-x')} \tag{A.4}$$

where in the last step we performed the transformation $k \to \hbar\nu_F k$. The denominator can now be rewritten as $(E^2 - k^2 - \Delta^2) = (\sqrt{E^2-\Delta^2} - k)(\sqrt{E^2-\Delta^2} + k)$ and we can see the two poles $\pm\sqrt{E^2-\Delta^2}$. Here we have to remember that the energy carries a infinitesimal imaginary part, that shifts the poles into the complex plane. For $E > 0$ the resulting imaginary part after taking the square root is bigger than 0 and the positive square root lies in the upper half-plane, while the negative one lies in the lower half-plane. When E switches sign, so does the imaginary part and for $E < 0$ the positive and negative pole lay in the lower and upper half-plane respectively. This will introduce a $\theta(E)$ in the calculation of the residues.

To calculate the line integral over the real k-axis we complete the contour and use the residue theorem. Depending on the sign of $x - x'$ we need to complete the contour in the upper or lower half-plane such that $\exp(ik(x-x'))$ vanishes for large k. That means for $x - x' > 0$ we need $\operatorname{Im} k > 0$ so the real part of the exponent is smaller than zero and the contour vanishes in the upper half-plane. Conversely, for $x - x' < 0$ we need $\operatorname{Im} k < 0$ and need to complete the contour in the lower half-plane. Now keeping track of the position of the poles as mentioned above we get

$$G(x,x',E) = \frac{1}{\hbar\nu_F} \int_{-\infty}^{\infty} \frac{\mathrm{d}k}{2\pi} \frac{E + k\sigma_z + \Delta\sigma_x}{E^2 - k^2 - \Delta^2} e^{\mathrm{i}\frac{k}{\hbar\nu_F}(x-x')} \tag{A.5}$$

$$= \frac{i}{\hbar\nu_F} \left[\text{Res(pole in upper half-plane)}\theta(x-x') \right.$$
$$\left. - \text{Res(poles in lower half-plane)}(1-\theta(x-x')) \right]. \tag{A.6}$$

The residues for a simple pole z of a function f can be calculated according to $\mathrm{Res_f(z)} =$

$\lim_{x\to z}(x-z)f(x)$. This leads to

$$\begin{aligned} G(x,x',E) = & -\frac{i}{\hbar\nu_F}\left[\left(\frac{E+\sqrt{E^2-\Delta^2}\sigma_z+\Delta\sigma_x}{2\sqrt{E^2-\Delta^2}}e^{\mathrm{i}\frac{\sqrt{E^2-\Delta^2}}{\hbar\nu_F}(x-x')}\theta(E)\right.\right. \\ & \left.\left.-\frac{E-\sqrt{E^2-\Delta^2}\sigma_z+\Delta\sigma_x}{2\sqrt{E^2-\Delta^2}}e^{-\mathrm{i}\frac{\sqrt{E^2-\Delta^2}}{\hbar\nu_F}(x-x')}(1-\theta(E))\right)\theta(x-x') \right. \\ & +\left(\frac{E-\sqrt{E^2-\Delta^2}\sigma_z+\Delta\sigma_x}{2\sqrt{E^2-\Delta^2}}e^{\mathrm{i}\frac{\sqrt{E^2-\Delta^2}}{\hbar\nu_F}(x-x')}\theta(E)\right. \\ & \left.\left.-\frac{E+\sqrt{E^2-\Delta^2}\sigma_z+\Delta\sigma_x}{2\sqrt{E^2-\Delta^2}}e^{-\mathrm{i}\frac{\sqrt{E^2-\Delta^2}}{\hbar\nu_F}(x-x')}(1-\theta(E))\right)\right. \\ & \left.\times\,(1-\theta(x-x'))\right], \end{aligned} \tag{A.7}$$

from which we can calculate the density of states according to

$$\mathcal{D}(E) = -\mathrm{Im}\left(\frac{\mathrm{Tr}\,G(x,x,E)}{\pi}\right). \tag{A.8}$$

Remembering that the Pauli matrices are traceless and evaluating the Heaviside function in a weak sense, i.e. $\theta(0)=1/2$, we find

$$\begin{aligned} \mathrm{Tr}\,G(x,x,E) = & -\frac{2i}{\hbar\nu_F}\left[\left(\frac{E}{2\sqrt{E^2-\Delta^2}}\theta(E)-\frac{E}{2\sqrt{E^2-\Delta^2}}(1-\theta(E))\right)\frac{1}{2}\right. \\ & \left.+\left(\frac{E}{2\sqrt{E^2-\Delta^2}}\theta(E)-\frac{E}{2\sqrt{E^2-\Delta^2}}(1-\theta(E))\right)\frac{1}{2}\right] \qquad \text{(A.9)} \\ = & -\frac{i}{\hbar\nu_F}\left[-\frac{E}{\sqrt{E^2-\Delta^2}}(1-2\theta(E))\right] \qquad \text{(A.10)} \end{aligned}$$

It can readily be seen that

$$-\frac{E}{\sqrt{E^2-\Delta^2}}(1-2\theta(E)) = \frac{|E|}{\sqrt{E^2-\Delta^2}} \tag{A.11}$$

and noticing that $\sqrt{E^2-\Delta^2}$ is imaginary for $E^2<\Delta^2$, we can write the density of states as

$$\mathcal{D}(E) = -\mathrm{Im}\left(\frac{\mathrm{Tr}\,G(x,x,E)}{\pi}\right) = \frac{1}{\pi\hbar\nu_F}\frac{|E|}{\sqrt{E^2-\Delta^2}}\,\theta(E^2-\Delta^2). \tag{A.12}$$

A.2 Free Green's function

The free Green's function in real-space is defined by the equation of motion

$$\left[E-(-i\hbar\nu_F\sigma_z\partial_x)\right]g_0(x,x',E) = \delta(x-x'). \tag{A.13}$$

Fourier-transformation to momentum domain yields

$$\left[E-\hbar\nu_F k\sigma_z\right]g_0(k,E) = 1, \tag{A.14}$$

which can easily be inverted to find

$$g_0(k,E) = \frac{1}{E-\hbar\nu_F k\sigma_z} = \begin{pmatrix} \frac{1}{E-\hbar\nu_F k} & 0 \\ 0 & \frac{1}{E+\hbar\nu_F k}\end{pmatrix}. \tag{A.15}$$

The inverse transformation can be performed element-wise. Formally we write

$$g(x,x',E) = \frac{1}{2\pi}\int_{-\infty}^{\infty} e^{ik(x-x')} g(k,E)\,\mathrm{d}k \tag{A.16}$$

$$= \frac{1}{2\pi}\begin{pmatrix} \int_{-\infty}^{\infty} \frac{e^{ik(x-x')}}{E-\hbar\nu_F k}\,\mathrm{d}k & 0 \\ 0 & \int_{-\infty}^{\infty} \frac{e^{ik(x-x')}}{E+\hbar\nu_F k}\,\mathrm{d}k \end{pmatrix} \tag{A.17}$$

and remember that by convention for the retarded Green's function the energy carries a infinitesimal positive imaginary part. That imaginary part shifts the pole into the complex k-plane such that we can apply the residue theorem. Just as in A.1 we now need to carefully keep track of the poles and complete the contour appropriately. Alternatively, one can note that this is just the above case with $\Delta = 0$ and we can use eq. (A.7) to find

$$\begin{aligned} g_0(x,x',E) = & -\frac{i}{\hbar\nu_F}\Bigg[\Bigg(\frac{E+E\sigma_z}{2E} e^{\mathrm{i}\frac{E}{\hbar\nu_F}(x-x')}\theta(E) \\ & - \frac{E-E\sigma_z}{2E} e^{-\mathrm{i}\frac{E}{\hbar\nu_F}(x-x')}(1-\theta(E))\Bigg)\theta(x-x') \\ & + \Bigg(\frac{E-E\sigma_z}{2E} e^{\mathrm{i}\frac{E}{\hbar\nu_F}(x-x')}\theta(E) \\ & - \frac{E+E\sigma_z}{2E} e^{-\mathrm{i}\frac{E}{\hbar\nu_F}(x-x')}(1-\theta(E))\Bigg)(1-\theta(x-x'))\Bigg] \end{aligned} \tag{A.18}$$

$$\begin{aligned} = & \frac{-i}{2\hbar\nu_F}\Bigg[e^{\frac{E(x-x')}{\hbar\nu_F}}\theta(x-x')(1+\sigma_z) \\ & + e^{-\frac{E(x-x')}{\hbar\nu_F}}(1-\theta(x-x'))(1-\sigma_z)\Bigg], \end{aligned} \tag{A.19}$$

after cancelling the E and collecting the Heaviside functions.

B Explicit solution for a diagonally driven two-level system

Here the Fourier components of the Greens function for a diagonally driven two-level-system with the Hamiltonian

$$H = k\sigma_z + V\sigma_z \sin \Omega t \tag{B.1}$$

are calculated.

B.1 Free problem

First solve the free propagation, where the equation of motion is

$$\left[\mathrm{i}\hbar\partial_t - k\sigma_z\right] g(t,t') = \delta(t-t') \tag{B.2}$$

and has the formal solution

$$g(t,t') = \exp\left(-\frac{\mathrm{i}}{\hbar}\int_{t'}^{t} \mathrm{d}\bar{t}\, k\sigma_z\right)\frac{\theta(t-t')}{\mathrm{i}\hbar} \tag{B.3}$$

$$= \exp\left(-\frac{\mathrm{i}}{\hbar}k\sigma_z(t-t')\right)\frac{\theta(t-t')}{\mathrm{i}\hbar} = g(t-t'). \tag{B.4}$$

It only depends on the difference $t-t'$, and we can calculate the Fourier transform

$$\tilde{g}(t,E) = \int \mathrm{d}\tau\, e^{\mathrm{i}\frac{E}{\hbar}\tau} g(t,t-\tau) \tag{B.5}$$

$$= \int \mathrm{d}\tau\, e^{\mathrm{i}\frac{E}{\hbar}\tau} g(\tau) \tag{B.6}$$

$$= \tilde{g}(E). \tag{B.7}$$

Remembering that E carries an infinitesimal imaginary part for convergence we can explicitly calculate this as

$$\tilde{g}(E) = \int \mathrm{d}\tau\, e^{\mathrm{i}\frac{E}{\hbar}\tau} \exp\left(-\frac{\mathrm{i}}{\hbar}k\sigma_z\tau\right)\frac{\theta(\tau)}{\mathrm{i}\hbar} \tag{B.8}$$

$$= \frac{1}{\mathrm{i}\hbar}\int_0^\infty \mathrm{d}\tau\, \exp\left(\frac{\mathrm{i}}{\hbar}(E-k\sigma_z)\tau\right) \tag{B.9}$$

$$= 0 - \frac{1}{\mathrm{i}\hbar}\left(\frac{\hbar}{\mathrm{i}}\frac{1}{E-k\sigma_z}\right) \tag{B.10}$$

$$= \frac{1}{E-k\sigma_z} \tag{B.11}$$

$$= \begin{pmatrix} \frac{1}{E-k} & 0 \\ 0 & \frac{1}{E+k} \end{pmatrix} \tag{B.12}$$

B.2 Full system

The full equation of motion is

$$\left[\mathrm{i}\hbar\partial_t - (k\sigma_z + V\sigma_z \sin \Omega t)\right] G(t,t') = \delta(t-t') \tag{B.13}$$

with the formal solution

$$G(t,t') = \exp\left(-\frac{\mathrm{i}}{\hbar}\int_{t'}^{t} \mathrm{d}\bar{t}\,(k\sigma_z + V\sigma_z \sin\Omega\bar{t})\right)\frac{\theta(t-t')}{\mathrm{i}\hbar} \tag{B.14}$$

$$= \exp\left(-\frac{\mathrm{i}}{\hbar}\int_{t'}^{t} \mathrm{d}\bar{t}\, V\sigma_z \sin\Omega\bar{t}\right)\underbrace{\exp\left(-\frac{\mathrm{i}}{\hbar}k\sigma_z(t-t')\right)\frac{\theta(t-t')}{\mathrm{i}\hbar}}_{=g(t-t')} \tag{B.15}$$

$$= \exp\left(-\frac{\mathrm{i}}{\hbar}V\sigma_z\left(\frac{-cos\Omega t}{\Omega}+\frac{cos\Omega t'}{\Omega}\right)\right)g(t-t') \tag{B.16}$$

$$= \exp\left(\mathrm{i}\frac{V\sigma_z}{\hbar\Omega}cos\Omega t\right)\exp\left(-\mathrm{i}\frac{V\sigma_z}{\hbar\Omega}cos\Omega t'\right)g(t-t'). \tag{B.17}$$

The exponentials can be written as sums of Bessel functions according to

$$\exp(\mathrm{i}z\cos\phi) = \sum_{n\in\mathbb{Z}} \mathrm{i}^n J_n(z) e^{\mathrm{i}n\phi}, \tag{B.18}$$

giving

$$G(t,t') = \sum_{k,l} \mathrm{i}^{k+l} J_k(\tilde{V}) J_l(-\tilde{V}) e^{\mathrm{i}k\Omega t} e^{\mathrm{i}l\Omega t'} g(t-t'), \tag{B.19}$$

where $\tilde{V} = \frac{V\sigma_z}{\hbar\Omega}$ and the Bessel functions of the matrices have to be understood as

$$J_k\left(\frac{V\sigma_z}{\hbar\Omega}\right) = \begin{pmatrix} J_k\left(\frac{V}{\hbar\Omega}\right) & 0 \\ 0 & J_k\left(-\frac{V}{\hbar\Omega}\right)\end{pmatrix}. \tag{B.20}$$

Setting $t' = t - \tau$, we can write

$$G(t,t-\tau) = \sum_{k,l} \mathrm{i}^{k+l} J_k(\tilde{V}) J_l(-\tilde{V}) \underbrace{e^{\mathrm{i}(k+l)\Omega t}}_{\text{(I)}} \underbrace{e^{-\mathrm{i}l\Omega\tau} g(\tau)}_{\text{(II)}}, \tag{B.21}$$

and observe some properties of G. The only t-dependent part is (I), which is periodic with $T = \frac{2\pi}{\Omega}$, so we can write this as a Fourier-series in t. The τ-dependent part (II) is not necessarily periodic, but its independent of t. The Fourier transform will result in a shifted $\tilde{g}$ in this part.

Performing the Fourier transform results in

$$\tilde{G}(t,E) = \int \mathrm{d}\tau\, e^{\mathrm{i}\frac{E}{\hbar}\tau} G(t,t-\tau) \tag{B.22}$$

$$= \sum_{k,l} \mathrm{i}^{k+l} J_k(\tilde{V}) J_l(-\tilde{V}) e^{\mathrm{i}(k+l)\Omega t} \int \mathrm{d}\tau\, e^{\mathrm{i}\frac{E-l\hbar\Omega}{\hbar}\tau} g(\tau) \tag{B.23}$$

$$= \sum_{k,l} \mathrm{i}^{k+l} J_k(\tilde{V}) J_l(-\tilde{V}) e^{\mathrm{i}(k+l)\Omega t} \tilde{g}(E - l\hbar\Omega). \tag{B.24}$$

From this we can calculate the Fourier components via Eq. (3.12) as

$$\tilde{G}_n(E) = \frac{1}{T}\int_0^T \mathrm{d}t\, e^{-\mathrm{i}n\Omega t}\tilde{G}(t,E) \tag{B.25}$$

$$= \sum_{k,l} \mathrm{i}^{k+l} J_k(\tilde{V}) J_l(-\tilde{V}) \underbrace{\frac{1}{T}\int_0^T \mathrm{d}t\, e^{\mathrm{i}(k+l-n)\Omega t}}_{=\delta_{n,k+l}=\delta_{n-l,k}} \tilde{g}(E - l\hbar\Omega) \tag{B.26}$$

$$= \mathrm{i}^n \sum_l J_{n-l}\left(\frac{V\sigma_z}{\hbar\Omega}\right) J_l\left(-\frac{V\sigma_z}{\hbar\Omega}\right) \tilde{g}(E - l\hbar\Omega) \tag{B.27}$$

C Impurity averaging

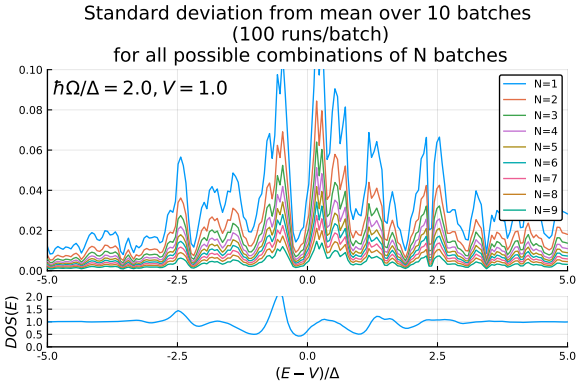

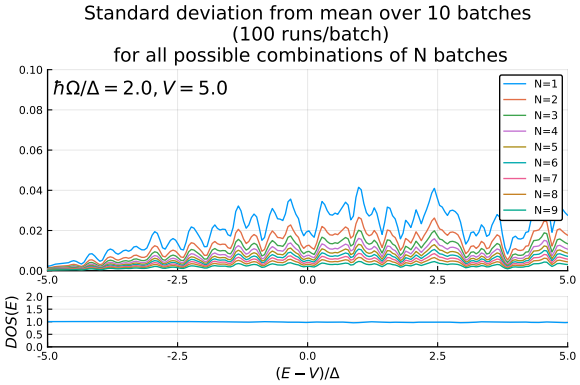

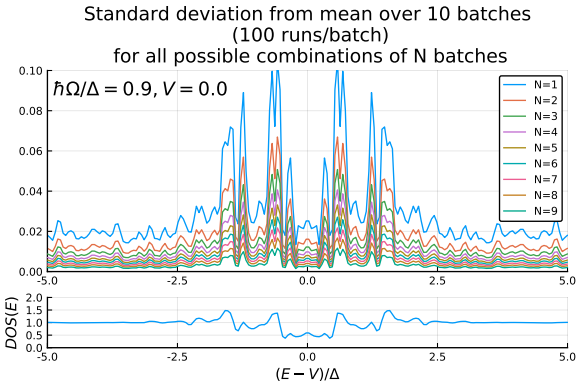

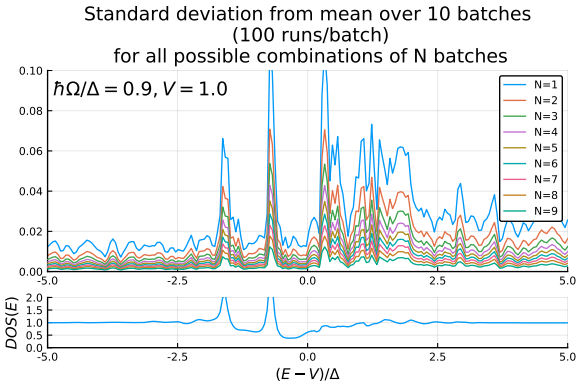

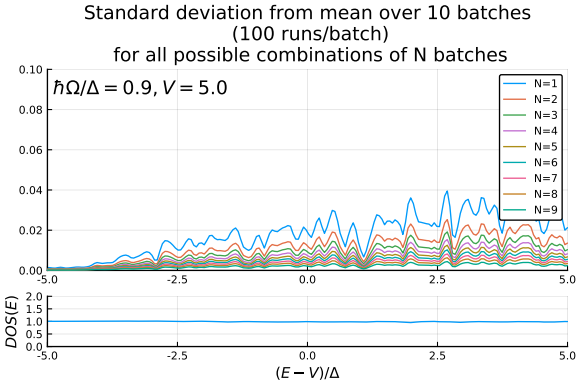

D Code

The implementation of the numeric model has been done for Julia 1.3.x . Julia is relatively new language created with speed and ease of use in mind. The main arguments to use it here was the easy syntax and the speed, that seems to be comparable or even faster than C for some cases. For more information see the documentation at https://docs.julialang.org/en/v1/

The code below is the source code to define a module that contains all the necessary functions to run numeric model. Effectively one simply has call the module and run the function "impurityaverage" with the desired parameters.

```
module EdgeImp
############################################################
# packages needed
using Distributed # for paralellization
using LinearAlgebra
using SharedArrays # for variables in parallel map
using DelimitedFiles # for writing in files
using Dates # for dates, e.g. in logfile
############################################################
# functions to export
export g # unperturbed Green's function in position representation
export Gndirect # Matrix GF equation and solution
export Mimpsingle # single impurity potential matrix/FCs
export Mimp # Nimp equal, aligned impurities potential matrix/FCs
export impurityaverage # impurity averaging function
############################################################

# Pauli matricies
sigma0=Matrix{ComplexF64}(I, 2, 2)
sigmax=Matrix{ComplexF64}([0.0 1.0; 1.0 0.0])
sigmay=Matrix{ComplexF64}([0.0 -im; im 0.0])
sigmaz=Matrix{ComplexF64}([1.0 0.0; 0.0 -1.0])
# vector containing the pauli matrices
sigma=[[sigmax];[sigmay];[sigmaz]]

# Inputs and typical values
# LolB=8.0 # system length parameter
# omega=1.0 # driving frequency in units of the gap
# nmax=3 # index of highest Fourier components -> 2nmax+1 total FCs
# Nruns=100 # No. of impurity averaging runs
# V=0.0 # potential strength of the imps relative to M
# M=0.1 # magnetic strength of the imps in units of \hbar\nu_F
# Emax=5.0 # Energy around gap center
# Enum=101 # No. of energy points

# free GF for impurity system
##### unperturbed Green's function sub matrices in position representation #####
function gR_V(E,u,up,LolB,V,Xvec)
    ########################################################
    # E: Energy scaled in units of Delta                   #
    # u=x/L impurity position relative to L                #
    # up=x'/L impurity position relative to L              #
    # LolB: L/l_B ratio system length/decay length, controls magnetic impurity
        ↪ strength    #
    # V: potential part of the impurity potential relative to M
        ↪                                #
    # Xvec: impurity vector containing impurity positions relative to L
        ↪                    #
    ########################################################
    #initialize empty matrix
    gR=zeros(ComplexF64,2,2)
    # Extract number of impurities
    N=size(Xvec)[1]
    # Heaviside function
    epsilon=1e-9 # Parameter controlling the Heaviside "sharpness" or width
    HS=0.50*(1.0+(2.0*atan((u-up)/epsilon)/pi))  # Smooth Heaviside of width
```

```
        ↪ epsilon
    # free impurity g
    gR[1,1]=-im*exp( im*E*LolB*(u-up))*HS
    gR[2,2]=-im*exp(-im*E*LolB*(u-up))*(1.0-HS)
    # Calculate phase factor due do potential part
    Theta =0.0
    Thetap=0.0
    for n=1:N
        Theta =Theta +V*(LolB/N)*0.50*(1.0+(2.0*atan((u-Xvec[n])/epsilon)/pi))
    Thetap=Thetap+V*(LolB/N)*0.50*(1.0+(2.0*atan((up-Xvec[n])/epsilon)/pi))
    end
    # in matrices
    expTheta=[exp(-im*Theta) 0.0; 0.0 exp(im*Theta)]
    expThetap=[exp(im*Thetap) 0.0; 0.0 exp(-im*Thetap)]
    # return g0 with proper phase factors
    return expTheta*gR*expThetap
end
##### unperturbed Green's function in position representation, fill with
    ↪ submatrices #####
function g(E,Xvec,LolB,V)
    ############################################################
    # E: Energy scaled in units of Delta                       #
    # LolB: L/l_B ratio system length/decay length, controls magnetic impurity
        ↪ strength    #
    # V: potential part of the impurity potential relative to M
        ↪                              #
    # Xvec: impurity vector containing impurity positions relative to L
        ↪                         #
    ############################################################
    Nimp=length(Xvec) # number of impurities
    g0=Matrix{ComplexF64}(undef, 2*Nimp, 2*Nimp) # initialize empty matrix
    # fill up with the submatrices
    for i=1:Nimp, j=1:Nimp
        xi=Xvec[i]
        xj=Xvec[j]
        g0[2*i-1:2*i,2*j-1:2*j]=gR_V(E,xi,xj,LolB,V,Xvec)
    end
    return g0
end

# set up and solving of matrix GF equation
function Gndirect(g1::Function,V0,Vp,Vm,omega,En,nmax,Xvec...)
    ############################################################
    # g1: "free" greens function (!!!first argument needs to be the Energy!!!,
        ↪ rest in Xvec...   #
    # in order of arguments of g1)
        ↪                                                      #
    # V0, Vp, Vm: 0th, 1st, -1st Fourier component of the impurity potential (
        ↪ matching the GF)   #
    # omega: driving frequency, scaled as (\hbar omega)/Delta
        ↪                                      #
    # En: Energy in units of Delta                             #
    # nmax: biggest fourier index, number of fourier modes=2*nmax+1 (n from -
        ↪ nmax:nmax)          #
    # Xvec... : remaining arguments of g1 other than the energy argument
        ↪                            #
    ############################################################
    ## set up matrix for matrix eq. ##
    gfsize=size(g1(En,Xvec...))[1] # size of the submatrices
    Id=Matrix{ComplexF64}(I,gfsize,gfsize) # unit matrix of GFsize
    A=zeros(ComplexF64,gfsize*(2*nmax+1),gfsize*(2*nmax+1)) #initialize matrix
        ↪ of the correct size 2nmax+1 blocks for -/0/+ components, blocksize=
        ↪ gfsize
    for n=-nmax:nmax-1 #loop over block main/upper/lower diagonal
        # diagonal
        A[1+(n+nmax)*gfsize:gfsize+(n+nmax)*gfsize,1+(n+nmax)*gfsize:gfsize+(n+
            ↪ nmax)*gfsize]=(Id-g1(En-n*omega,Xvec...)*V0)
        # upper minor diagonal
        A[1+(n+nmax)*gfsize:gfsize+(n+nmax)*gfsize,1+(n+1+nmax)*gfsize:gfsize+(n
            ↪ +1+nmax)*gfsize]=-g1(En-n*omega,Xvec...)*Vm
        # lower minor diagonal
        A[1+(n+1+nmax)*gfsize:gfsize+(n+1+nmax)*gfsize,1+(n+nmax)*gfsize:gfsize+
            ↪ (n+nmax)*gfsize]=-g1(En-(n+1)*omega,Xvec...)*Vp
```

```
    end
    # last diagonal block
    A[1+(2*nmax)*gfsize:gfsize+(2*nmax)*gfsize,1+(2*nmax)*gfsize:gfsize+(2*nmax)
        ↪ *gfsize]=(Id-g1(En-nmax*omega,Xvec...)*V0)
    ########################
    ## set up right side of matrix eq. ##
    b=zeros(ComplexF64,gfsize*(2*nmax+1),gfsize)
    b[gfsize*nmax+1:gfsize*nmax+gfsize,1:gfsize]=g1(En,Xvec...)
    ########################
    ## solve matrix eq. ##
    Gn=\(A,b)
    ########################
    check=(norm(A*Gn-b),norm(Gn[(end-gfsize)+1:end,:])) # check if matrix
        ↪ inversion is sufficiently exact, check if fourier coefficient
        ↪ vanishes
    return (Gn,check)
end


##### creating impurity potentials and impurity distributions

# impurity potential matrices for aligned/equal imps !this is equal for all imp
    ↪ distributions, calc before imp avg loop!
# harmonic driving in x-z-plane
function Mimp(M,Nimp)
    ############################################################
    # M impurity stength                                       #
    # Nimp: number of impurities                               #
    ############################################################
    M0s=zeros(ComplexF64,2,2) # 0th FC singel imp
    Mps=M/(2*im)*(sigmax+im*sigmaz) # 1st FC singel imp
    Mms=Mps' # -1st FC singel imp
    M0,Mp,Mm=map(x->kron(Matrix{ComplexF64}(I,Nimp,Nimp),x),(M0s,Mps,Mms)) #
        ↪ kronecker product for M, 2x2 matrix on diag of big matrix, map on
        ↪ three matrices
    # returns (0th, 1st, -1st) Fourier component of the big matrix in that order
    return M0,Mp,Mm
end
# from arbitrary single impurity potential
function Mimp(M0s,Mps,Mms,Nimp)
    ############################################################
    # M0,Mps,Mms: single impurity FCs                          #
    # Nimp: number of impurities                               #
    ############################################################
    M0,Mp,Mm=map(x->kron(Matrix{ComplexF64}(I,Nimp,Nimp),x),(M0s,Mps,Mms)) #
        ↪ kronecker product for M, 2x2 matrix on diag of big matrix, map on
        ↪ three matrices
    # returns (0th, 1st, -1st) Fourier component of the big matrix in that order
    return M0,Mp,Mm
end

# create 2x2 single impurity matrix fourier coefficients for rotation in x-z-
    ↪ plane
function Mimpsingle(M)
    M0=zeros(ComplexF64,2,2)
    Mp=M/(2*im)*(sigmax+im*sigmaz)
    Mm=Mp'
    return (M0,Mp,Mm)
end

# create random impurity distribution
function imps(Nimp)
   # create random impurity positions
    #srand(2) # Set the random seed
    Xvec=rand(Float64,Nimp)
    sort!(Xvec)  # sort the impurity position
    minimaldistance=minimum(Xvec[2:Nimp]-Xvec[1:Nimp-1])
    # Make sure impurities are reasonably far apart
    while (minimaldistance<=10e-6)
    Xvec=rand(Float64,Nimp)
        sort!(Xvec)  # sort the impurity position
        minimaldistance=minimum(Xvec[2:Nimp]-Xvec[1:Nimp-1])
    end
```

```
    # find position and index of impurity closest to the center
    center=findmin(abs.(Xvec.-0.5))[2]
    return Xvec,center
end

##### impurity averaging #####
function impurityaverage(Nimp,Erange,M,V,omega,logfile::String,nmax=5,Nruns=100,
    ↪ LolB=8.0,Gnsolve::Function=Gndirect,gfree::Function=g;dyn::Bool=true,
    ↪ impdist::String="rand")
    # initialize matrix
    G=zeros(ComplexF64,2*(2*nmax+1),2*length(Erange))
    Gcheckmax=Array{Tuple{Float64,Float64},1}[]
    # if for dynamic/static
    if dyn==true
        M0,Mp,Mm=Mimp(M,Nimp) #dynamic imps
    elseif dyn==false
        M0s,Mps,Mms=sigmax*M,zeros(ComplexF64,2,2),zeros(ComplexF64,2,2) #static
            ↪  imps
        M0,Mp,Mm=map(x->kron(Matrix{ComplexF64}(I,Nimp,Nimp),x),(M0s,Mps,Mms))
    end
    # if for rand/eq
    if impdist=="rand" # random impurities
        for k in 1:Nruns # impurity averaging loop
            (Xvec,center)=imps(Nimp)
            ### ENERGY MAP/LOOP ###
            A=pmap(E->Gnsolve(gfree,M0,Mp,Mm,omega,E,nmax,Xvec,LolB,V),Erange)
            G+=reduce(hcat,[reduce(vcat,g[i*2*Nimp+(2*center-1):i*2*Nimp+(2*
                ↪ center),2*center-1:2*center] for i in 0:2*nmax) for g in
                ↪ first.(A)]) # extract 2x2 blocks for the center impurity
            Gcheckmax=vcat(Gcheckmax,(maximum(first.(last.(A))),maximum(last.(
                ↪ last.(A))))) # extract check values
            # write in logfile
            if mod(k,20)==0
                check1=maximum(first.(Gcheckmax))
                check2=maximum(last.(Gcheckmax))
                open(logfile,"a") do iolog
                    timestamp=now()
                    write(iolog, "[$timestamp]: finished $k of $Nruns impurity
                        ↪ averaging runs, biggest check values in the last
                        ↪ runs: inversion: $check1 , size of last Fourier
                        ↪ coefficient: $check2\n")
                    end # open
                Gcheckmax=Array{Tuple{Float64,Float64},1}[] # reset check values
            end # if
        end # imp loop
    elseif impdist=="eq" # equal distance imps. = barrier
        Xvec=range(0.0,stop=1.0,length=Nimp)
        center=findmin(abs.(Xvec.-0.5))[2]
        ### ENERGY MAP/LOOP ###
        A=pmap(E->Gnsolve(gfree,M0,Mp,Mm,omega,E,nmax,Xvec,LolB,V),Erange)
        G+=reduce(hcat,[reduce(vcat,g[i*2*Nimp+(2*center-1):i*2*Nimp+(2*center),
            ↪ 2*center-1:2*center] for i in 0:2*nmax) for g in first.(A)]) #
            ↪ extract 2x2 blocks for the center impurity
        check1=maximum(first.(last.(A)))
        check2=maximum(last.(last.(A)))
        # write in logfile
        open(logfile,"a") do iolog
            timestamp=now()
            write(iolog, "[$timestamp]: finished equally distributed impurities
                ↪ run, biggest check values: inversion: $check1 , size of last
                ↪  Fourier coefficient: $check2\n")
        end # open
    end # if
    return G/Nruns
end

end #module
```